PHYSICAL REVIEW D **81,** 084039 (2010)

Self-force on a scalar charge in Kerr spacetime: Circular equatorial orbits

Niels Warburton and Leor Barack

School of Mathematics, University of Southampton, Southampton SO17 1BJ, United Kingdom

(Received 9 March 2010; published 20 April 2010)

We present a calculation of the scalar-field self-force (SSF) acting on a scalar-charge particle in a strong-field orbit around a Kerr black hole. Our calculation specializes to circular and equatorial geodesic orbits. The analysis is an implementation of the standard mode-sum regularization scheme: We first calculate the multipole modes of the scalar-field perturbation using numerical integration in the frequency domain, and then apply a certain regularization procedure to each of the modes. The dissipative piece of the SSF is found to be consistent with the flux of energy and angular-momentum carried by the scalar waves through the event horizon and out to infinity. The conservative (radial) component of the SSF is calculated here for the first time. When the motion is retrograde this component is found to be repulsive (outward pointing, as in the Schwarzschild case) for any spin parameter a and (Boyer-Lindquist) orbital radius r_0. However, for prograde orbits we find that the radial SSF becomes attractive (inward pointing) for $r_0 > r_c(a)$, where r_c is a critical a-dependent radius at which the radial SSF vanishes. The dominant conservative effect of the SSF in Schwarzschild spacetime is known to be of third post-Newtonian (3PN) order (with a logarithmic running). Our numerical results suggest that the leading-order PN correction due to the black hole's spin arises from spin-orbit coupling at 3PN order, which dominates the overall SSF effect at large r_0. In PN language, the change of sign of the radial SSF is attributed to an interplay between the spin-orbit term ($\propto -ar_0^{-4.5}$) and the Schwarzschild term ($\propto r_0^{-5}\log r_0$).

DOI: 10.1103/PhysRevD.81.084039 PACS numbers: 04.25.Nx, 04.25.−g, 04.70.Bw

I. INTRODUCTION

The gravitational two-body problem is extremely difficult to tackle in a general-relativistic context, due to the intrinsic nonlinearities of the theory. However, when one of the two components is much more massive than the other, the problem simplifies and can sometimes be attacked via black hole perturbation theory. Nature provides us with such extreme mass-ratio systems in the form of compact objects inspiraling into massive black holes in galactic nuclei. Such systems are key targets for the planned space-based gravitational wave detector LISA (Laser Interferometer Space Antenna) [1]. Detection of the gravitational waves and accurate extraction of the physical parameters require precise theoretical templates of the waveforms, which, in turn, necessitate knowledge of the radiative evolution of the system.

The underlying theoretical problem, in its most fundamental form, is that of a pointlike particle orbiting a black hole of a much larger mass. The interaction of the particle with its own gravitational field gives rise to a gravitational self-force (GSF), which is responsible, in particular, for the radiative inspiral. How to calculate this GSF has been the subject of extensive study over the last decade [2]. The fundamental formalism for calculations of the GSF in curved spacetime was first laid down by Mino, Sasaki, and Tanaka [3] and independently by Quinn and Wald [4], with important later supplements by Detweiler and Whiting [5], Gralla and Wald [6], Pound [7], and Harte [8] (see Poisson for a review [9]). The resulting equations of motion are known as the MiSaTaQuWa equations. The analogous self-force equation of motion for the electromagnetic case was derived by DeWitt and Brehme long ago [10] (with corrections by Hobbs [11]) and reproduced more recently using other methods in [4,12]. Quinn obtained the equivalent results for the scalar-field self-force (SSF) [13].

The MiSaTaQuWa equations of motion are hard to implement directly and so they were later recast into forms more amenable to practical calculation. One of the standard methods is the mode-sum scheme first introduced in Ref. [14]. Using this method, self-force calculations have been performed for a range of problems. These include calculations of the SSF for radial infall [15], circular [16,17], and eccentric [18] orbits; the electromagnetic self-force for eccentric orbits [19]; and the GSF for radial infall [20], circular [21,22], and eccentric orbits [23]. More recently, researchers have been exploring alternative calculation methods which are based on direct regularization of the self-interaction in 2 + 1 and 3 + 1 dimensions [24–26]. Common to all calculations presented so far is the fact that they specialize to the simpler (but less astrophysically relevant) case where the central object is a nonrotating, Schwarzschild black hole.

In this paper we open a new front in self-force calculations by considering extreme mass-ratio systems where the central black hole is rotating. The motivation for this is clear: Although little is known about the spin distribution of astrophysical massive black holes (but see, e.g., [27,28]), there is no reason to think that massive holes in nature are nonrotating. Hence, a useful model of a LISA-relevant inspiral must incorporate a Kerr black hole as a

central object. Indeed, as this work demonstrates, the spin of the central hole may have a very pronounced effect on the value of the self-force and hence on the inspiral dynamics.

Computing the GSF for generic inspiral orbits about a Kerr black hole is an extremely challenging task, and this work only represents a first step toward this ultimate goal. The recent advance in calculations of the GSF in the Schwarzschild case [29] was achieved after nearly a decade of development, in which the necessary computational techniques had been devised mainly by using the SSF as a simple test bed. In preparing to tackle the Kerr problem, we once again resort here to the simplicity of the scalar-field toy model. Furthermore, as a primer, we specialize to (geodesic) orbits which are both circular and equatorial. This setup already captures much of the complexity of the Kerr problem (and, indeed, offers an opportunity to explore some qualitatively new physics), while providing a more manageable environment for development.

Our calculation represents a first application of the standard mode-sum scheme for orbits in a Kerr black hole. As such, it provides a first test of the regularization parameter values derived in Ref. [30] (we shall review the notion of regularization parameters in Sec. III below). We opt here to work in the frequency domain, with the obvious advantage that we then only need to deal with *ordinary* differential equations (ODEs). We decompose the scalar-field equation in a basis of spheroidal harmonics (which are frequency dependent), and solve the resulting ODEs numerically, with suitable boundary conditions. Since the mode-sum scheme requires as input the *spherical*-harmonic modes of the scalar-field gradient, we then need to reexpand the spheroidal-harmonic solutions into spherical-harmonic components. A major technical hurdle intrinsic to this procedure is that the discontinuity of the spherical-harmonic components across the particle's orbit hampers the convergence of the frequency series there, due to the Gibbs phenomenon. This problem was analyzed in depth in Ref. [31], and a simple and elegant solution was proposed, which entirely circumvents the problem. With this recent development, the frequency-domain approach becomes an attractive option for SSF studies, in our view. (We remark that the above Gibbs phenomenon issue does not manifest itself in the case of circular orbits considered in our current work.)

In this work we calculate the dissipative and conservative components of the SSF for a variety of orbital radii and black hole spins. Our results for the dissipative component are found to agree well with the numerical results of Gralla *et al.* [32] (computed from asymptotic fluxes), as well as with the analytic results of Gal'tsov [33] at large orbital radii. As a further important test of our code we verify that the work done by the dissipative component of the SSF precisely balances the flux of energy in the scalar waves radiated out to infinity and through the event horizon, as extracted from our numerical solutions. For the conservative component our code recovers the results of Diaz-Rivera *et al.* [17] in the Schwarzschild case. This conservative piece is calculated here for the first time for a nonzero Kerr spin parameter, revealing several interesting new features. Our main results for the conservative SSF are displayed in Fig. 5.

The remainder of this paper is structured as follows. In Sec. II we review the relevant features of circular-equatorial geodesics of the Kerr geometry, and describe the setup of our problem. In Sec. III we discuss the application of the mode-sum scheme for orbits about a Kerr black hole, attempted here for the first time. Section IV describes our numerical method, and in Sec. V we provide various validation tests of our code and present our results. Lastly, in Sec. VI we summarize our results and consider future work. Throughout this work we use Boyer-Lindquist coordinates (t, r, θ, ϕ), with metric signature $(-+++)$ and geometrized units such that the gravitational constant and the speed of light are equal to unity.

II. SETUP AND REVIEW OF PERTURBATION FORMALISM

A. Orbit and equation of motion

Consider a pointlike particle of mass μ and scalar charge q, set in motion about a Kerr black hole with mass M and spin aM. We assume $-M < a < M$, with negative values of a corresponding to retrograde orbits. We denote the particle's worldline (in Boyer-Lindquist coordinates) by $x_p^\mu(\tau)$ and its four-velocity by $u^\mu = dx_p^\mu/d\tau$, where τ is the proper time. In this work we neglect the GSF, and consider only the SSF, denoted $F^\alpha_{\rm self}(\propto q^2)$. Then, the particle's motion is governed by [13]

$$u^\beta \nabla_\beta(\mu u^\alpha) = F^\alpha_{\rm self}, \tag{1}$$

where the covariant derivative is taken (as elsewhere in this work) with respect to the background Kerr geometry. In this work we do not wish to consider the backreaction from the SSF on the particle's motion. Our goal is merely to calculate the SSF that would be felt by a particle fixed on a geodesic orbit. We envisage that this SSF information could be used to compute the orbital evolution as a second step, but here we do not attempt to carry out the evolution analysis. For simplicity, we specialize to motion along a geodesic which is both circular $[r_p(\tau) = r_0 = \text{const}]$ and equatorial $[\theta_p(\tau) \equiv \pi/2]$. Note that, due to the reflective symmetry of the Kerr metric about the equatorial plane, an initially equatorial orbit (with $\theta_p = \pi/2$ and $d\theta_p/d\tau = 0$ at some initial time) would remain so at all times, even under the influence of the SSF.

Following from the stationarity and axial symmetry of the background Kerr metric, there exist two Killing vectors, $\xi^\mu_{(t)} = dx^\mu/dt$ and $\xi^\mu_{(\phi)} = dx^\mu/d\phi$. The Kerr metric

also admits a Killing tensor $Q^{\mu\nu}$. To each of these there is associated a conserved quantity: the specific energy $\mathcal{E} = -\xi^{\mu}_{(t)}u_{\mu} = -u_t$, the specific azimuthal angular-momentum $\mathcal{L} = \xi^{\mu}_{(\phi)}u_{\mu} = u_{\phi}$, and the Carter constant $Q = Q^{\mu\nu}u_{\mu}u_{\nu}$. Given initial conditions, these three parameters completely specify the orbit of the test particle about the Kerr black hole.

For our circular and equatorial orbits, one readily finds by solving the geodesic equations (taking $\theta_p = \pi/2$ and $dr_p/d\tau = d^2r_p/d\tau^2 = 0$) [34]

$$\begin{aligned}\mathcal{E} &= \frac{1 - 2v^2 + \tilde{a}v^3}{\sqrt{1 - 3v^2 + 2\tilde{a}v^3}},\\ \mathcal{L} &= r_0 v \frac{1 - 2\tilde{a}v^3 + \tilde{a}^2v^4}{\sqrt{1 - 3v^2 + 2\tilde{a}v^3}},\end{aligned} \tag{2}$$

where $v \equiv \sqrt{M/r_0}$ and $\tilde{a} \equiv a/M$. The Carter constant is given explicitly by

$$Q = u_{\theta}^2 + \cos^2\theta_p[a^2(1 - \mathcal{E}^2) + \csc^2\theta_p\mathcal{L}^2], \tag{3}$$

and so it vanishes identically in our case. The angular frequency Ω_{ϕ} with respect to coordinate time t is given by

$$\Omega_{\phi} \equiv \frac{d\phi_p}{dt} = \frac{u^{\phi}}{u^t} = \frac{g^{\phi\phi}\mathcal{L} - g^{t\phi}\mathcal{E}}{g^{t\phi}\mathcal{L} - g^{tt}\mathcal{E}} = \frac{v^3}{M(1 + \tilde{a}v^3)}, \tag{4}$$

where hereafter $g_{\alpha\beta}$ denotes the Kerr background metric, here evaluated at the circular orbit. Notice our convention is that $\mathcal{L}$ and Ω_{ϕ} are always taken positive, with prograde/retrograde orbits distinguished by the sign of a ($a > 0$ for prograde, $a < 0$ for retrograde).

Note that in Eq. (1) we have kept the mass μ inside the derivative operator. Quinn [13] (see also Burko *et al.* [35]) discussed the fact that plausible action principles for the scalar charge in curved spacetime give rise to a dynamically varying mass. In general, the evolution of the mass is governed by the SSF component tangent to u^{α}:

$$\frac{d\mu}{d\tau} = -u^{\alpha}F_{\alpha}. \tag{5}$$

In our stationary, circular-orbit setup, however, we must have $d\mu/d\tau = 0$. Therefore $u^{\alpha}F_{\alpha} = 0$ or, more explicitly,

$$F_t + \Omega_{\phi}F_{\phi} = 0. \tag{6}$$

This trivial relation between F_t and F_{ϕ} means that in our analysis we need only compute one of these components.

B. Scalar-field equation and multipole decomposition

We assume that the particle's field Φ can be treated as a small perturbation over the fixed Kerr geometry, and that it obeys the minimally coupled Klein-Gordon equation

$$\nabla_{\alpha}\nabla^{\alpha}\Phi = -4\pi T, \tag{7}$$

sourced by the particle's scalar-charge density T. We model this energy-momentum as a δ-function distribution along the particle's worldline, in the form

$$\begin{aligned}T &= q\int \delta^4(x^{\mu} - x^{\mu}_p(\tau))[-g(x)]^{-1/2}d\tau\\ &= \frac{q}{r_0^2u^t}\delta(r - r_0)\delta(\phi - \phi_p)\delta(\theta - \pi/2),\end{aligned} \tag{8}$$

where $g = -\rho^4\sin^2\theta$ is the metric determinant, and where in the second equality we have specialized to $r_p = r_0$ and $\theta_p = \pi/2$. The four-velocity component u^t is related to the particle's energy and angular-momentum through $u^t = g^{t\phi}\mathcal{L} - g^{tt}\mathcal{E}$.

Carter discovered [36] that the scalar wave equation (7) was completely separable in Kerr geometry, with Brill *et al.* giving the explicit separation formula [37]. We follow their method and decompose the field into spheroidal harmonics and frequency modes in the form

$$\Phi = \int\sum_{\hat{l}=0}^{\infty}\sum_{m=-\hat{l}}^{\hat{l}} R_{\hat{l}m\omega}(r)S_{\hat{l}m}(\theta;\sigma^2)e^{im\phi}e^{-i\omega t}d\omega. \tag{9}$$

Here $S_{\hat{l}m}(\theta;\sigma^2)$ are spheroidal Legendre functions with (ω-dependent) spheroidicity σ^2 [we reserve the term *spheroidal harmonic* for the product $S_{\hat{l}m}(\theta;\sigma^2)e^{im\phi}$]. We label the spheroidal Legendre function by $\hat{l}m$, as we will later introduce *spherical* harmonics which we label by lm. The spheroidal harmonics are orthonormal, with normalization given by

$$\oint S_{\hat{l}m}(\theta;\sigma^2)e^{im\phi}S_{\hat{l}'m'}(\theta;\sigma^2)e^{-im'\phi}d\Omega = \delta_{\hat{l}\hat{l}'}\delta_{mm'}, \tag{10}$$

where the integration is over a two-sphere t, $r = $ const with area element $d\Omega = \sin\theta d\theta d\phi$, and $\delta_{n_1n_2}$ is the standard Kronecker delta.

The source term in Eq. (7) is decomposed in a similar manner, writing

$$\rho^2T = \int\sum_{\hat{l}=0}^{\infty}\sum_{m=-\hat{l}}^{\hat{l}} \tilde{T}_{\hat{l}m\omega}(r)S_{\hat{l}m}(\theta;\sigma^2)e^{im\phi}e^{-i\omega t}d\omega, \tag{11}$$

where the factor $\rho^2 \equiv r^2 + a^2\cos^2\theta$ is inserted for later convenience. The periodicity of circular orbits implies that the spectrum of the Fourier transform in Eqs. (9) and (11) is given, in our case, by $\omega = n\Omega_{\phi} \equiv \omega_n$ for integer n. Hence for circular-equatorial orbits ($r_p = r_0$, $\theta_p = \pi/2$, $\phi_p = \Omega_{\phi}t$) $\tilde{T}_{\hat{l}m\omega}$ is given explicitly by

$$\begin{aligned}\tilde{T}_{\hat{l}m\omega_n}(r) &= \frac{\Omega_{\phi}}{2\pi}\int_0^{2\pi/\Omega_{\phi}} S_{\hat{l}m}(\theta;\sigma^2)\rho^2Te^{i(n-m)\Omega_{\phi}t}dt\\ &= \frac{q}{u^t}S_{\hat{l}m}(\pi/2;\sigma^2)\delta(r - r_0)\delta^n_m,\end{aligned} \tag{12}$$

where in the second line we have substituted for T from Eq. (8). Thus, each m mode contains a single n harmonic, and the spectrum is given by $\omega_n = \omega_m$ with

$$\omega_m \equiv m\Omega_\phi. \tag{13}$$

Substituting the field and source decompositions into the field equation (7), we subsequently find the radial and angular equations to be

$$\Delta\frac{\partial}{\partial r}\left(\Delta\frac{\partial R_{\hat{l}m\omega_m}}{\partial r}\right)+[a^2m^2-4Mrma\omega_m+(r^2+a^2)^2\omega_m^2 - a^2\omega_m^2\Delta-\lambda_{\hat{l}m}\Delta)]R_{\hat{l}m\omega_m}=-4\pi\Delta_0\tilde{T}_{\hat{l}m\omega_m}(r), \tag{14}$$

$$\frac{1}{\sin\theta}\frac{\partial}{\partial\theta}\left(\sin\theta\frac{\partial S_{\hat{l}m}}{\partial\theta}\right)+\left(\lambda_{\hat{l}m}+a^2\omega_m^2\cos^2\theta-\frac{m^2}{\sin^2\theta}\right)S_{\hat{l}m}=0, \tag{15}$$

where $\Delta\equiv r^2-2Mr+a^2$ and $\Delta_0\equiv\Delta(r_0)$. The angular equation (15) takes the form of the spheroidal Legendre equation with spheroidicity $\sigma^2=-a^2\omega_m^2$. Its eigenfunctions are the spheroidal Legendre functions $S_{\hat{l}m}(\theta;-a^2\omega_m^2)$ and its eigenvalues are denoted by $\lambda_{\hat{l}m}$. In general, there is no closed form for $S_{\hat{l}m}$ or $\lambda_{\hat{l}m}$ but they can be calculated using the spherical-harmonic decomposition method described in Appendix A. When $a=0$ the spheroidal harmonics $S_{\hat{l}m}e^{im\phi}$ coincide with their spherical counterparts $Y_{\hat{l}m}$, and their eigenvalues reduce to $\lambda_{\hat{l}m}=\hat{l}(\hat{l}+1)$.

As noted by Bardeen *et al.* [38] the radial equation (14) can be simplified by transforming to a new variable,

$$\psi_{\hat{l}m\omega_m}(r)\equiv rR_{\hat{l}m\omega_m}(r), \tag{16}$$

and introducing the tortoise radial coordinate r_* defined through

$$\frac{dr_*}{dr}=\frac{r^2}{\Delta}. \tag{17}$$

With the above definition the tortoise coordinate is given explicitly in terms of r as

$$r_*=r+M\ln(\Delta/M^2)+\frac{(2M^2-a^2)}{2(M^2-a^2)^{1/2}}\ln\left(\frac{r-r_+}{r-r_-}\right), \tag{18}$$

where we have specified the constant of integration and $r_\pm=M\pm\sqrt{M^2-a^2}$ are the outer and inner roots, respectively, of the equation $\Delta=0$. We note that there is an alternative common choice for the tortoise coordinate, namely,

$$\frac{d\tilde{r}_*}{dr}=\frac{r^2+a^2}{\Delta}, \tag{19}$$

which is useful in that $v\equiv t+\tilde{r}_*$ and $u\equiv t-\tilde{r}_*$ are then associated with the "ingoing" and "outgoing" principal null congruences of the Kerr background [39]. We shall later refer to $\tilde{r}_*$ in discussing boundary conditions, but for our field equation we opt to adopt the coordinate r_*, as the $\tilde{r}_*$ coordinate leads to a more complicated radial potential [37]. In terms of $\psi_{\hat{l}m\omega_m}(r)$ and r_*, the radial equation (14) takes the simpler form

$$\frac{d^2\psi_{\hat{l}m\omega_m}}{dr_*^2}+W_{\hat{l}m\omega_m}(r)\psi_{\hat{l}m\omega_m}=-\frac{4\pi q\Delta_0}{r_0^3u^t}S_{\hat{l}m}(\pi/2;-a^2\omega_m^2)\delta(r-r_0), \tag{20}$$

where we have substituted for the source from Eq. (12) and where $W_{\hat{l}m\omega_m}$ is an effective (ω-dependent) radial potential given by

$$W_{\hat{l}m\omega_m}(r)=\left[\frac{(r^2+a^2)\omega_m-am}{r^2}\right]^2-\frac{\Delta}{r^4}\left[\lambda_{\hat{l}m}-2am\omega_m+a^2\omega_m^2+\frac{2(Mr-a^2)}{r^2}\right]. \tag{21}$$

In the case of circular-equatorial orbits, axially symmetric modes (i.e., ones with $m=0$) have vanishing spheroidicity and $\lambda_{\hat{l},m=0}=\hat{l}(\hat{l}+1)$. The radial equation (20) then admits a simple analytic solution. It is given by

$$\psi_{\hat{l},m=0}=\begin{cases}\tilde{\alpha}_{\hat{l}}rQ_{\hat{l}}(x_0)P_{\hat{l}}(x) & r\le r_0\\ \tilde{\alpha}_{\hat{l}}rP_{\hat{l}}(x_0)Q_{\hat{l}}(x) & r\ge r_0,\end{cases} \tag{22}$$

where

$$x\equiv\beta(r-M)\quad\text{and}\quad\beta\equiv\sqrt{\frac{M^2+a^2}{M^4-a^4}}, \tag{23}$$

with $x_0\equiv x(r_0)$ and $P_{\hat{l}}$ and $Q_{\hat{l}}$ being the Legendre polynomials of the first and second kinds, respectively. The coefficient $\alpha_{\hat{l}}$ is derived from the jump condition in the derivative of the field at the location of the particle and is given explicitly by

$$\tilde{\alpha}_{\hat{l}}=\frac{-4\pi q(u^t\beta\Delta_0)^{-1}S_{\hat{l}0}(\pi/2;0)}{Q'_{\hat{l}}(x_0)P_{\hat{l}}(x_0)-P'_{\hat{l}}(x_0)Q_{\hat{l}}(x_0)}, \tag{24}$$

where a prime denotes differentiation with respect to x.

C. Boundary conditions

Equation (20) determines the radial field $\psi(r)$ anywhere outside the black hole once boundary conditions are specified on the horizon ($r_*\to-\infty$) and at spatial infinity ($r_*\to\infty$). The boundary conditions follow from physical considerations: At the event horizon radiation should be ingoing, and at spatial infinity radiation should be outgoing (in a sense made precise below). As we approach the boundaries the potential $W(r)$ in the radial equation approaches a constant value and the equation becomes that of a simple harmonic oscillator with frequencies

$$W^{1/2}(r_*\to\infty)=\omega_m, \tag{25}$$

$$W^{1/2}(r_*\to-\infty)=\frac{2Mr_+\omega_m-am}{r_+^2}\equiv\gamma_m. \tag{26}$$

Recalling Eq. (9) we observe that, at infinity, the t, r

dependence of the $\hat{l}m\omega$-mode contribution to the full field Φ will have the asymptotic form $\Phi_{\hat{l}m\omega} \sim \exp[-i\omega_m(t \pm \tilde{r}_*)]/r$, where we have converted from r_* to $\tilde{r}_*$ by noting that the two coincide (up to an additive constant) at $r_* \to \infty$. Choosing the sign such that the exponent is expressed in terms of the retarded time coordinate $u = t - \tilde{r}_*$ ensures that any radiation will be purely outgoing at infinity. Hence the lower sign applies, and the correct asymptotic boundary condition for the radial field is given by

$$\psi_{\hat{l}m\omega}(r_* \to \infty) \sim e^{+i\omega_m r_*}. \tag{27}$$

At the horizon the situation is slightly more delicate. The asymptotic radial solutions admit the form $\psi_{\hat{l}m\omega} \sim \exp(\pm i\gamma_m r_*) \sim \exp[\pm i(\omega_m - m\Omega_+)\tilde{r}_*]$, where we have expressed r_* in terms of $\tilde{r}_*$ using the asymptotic relation $r_* \to [r_+/(2M)]\tilde{r}_* + \text{const}$ as $r_* \to -\infty$, and defined

$$\Omega_+ \equiv \frac{a}{2Mr_+}. \tag{28}$$

(The frequency Ω_+ is the angular velocity Ω_ϕ of a stationary observer just outside the event horizon, and might be interpreted as the angular velocity of the black hole itself [39].) In evaluating the $\hat{l}m\omega$-mode contribution to the full field Φ at the horizon, one must now exercise care, and recall that the Boyer-Lindquist coordinate ϕ is *singular* at the horizon [39], and hence the factor $\exp(im\phi)$ in Eq. (9) is singular, too. We must instead express the field in terms of a regular azimuthal coordinate, and, following [40], we introduce

$$\phi_+ \equiv \phi - \Omega_+ t. \tag{29}$$

In terms of the regular coordinate ϕ_+ we obtain, as $r_* \to -\infty$, $\Phi_{\hat{l}m\omega} \sim \exp[im\phi_+ - i(\omega_m - m\Omega_+)(t \mp \tilde{r}_*)]$, where $\mp$ correspond to $\pm$ in the radial solutions $\psi_{\hat{l}m\omega} \sim \exp(\pm i\gamma_m r_*)$. For this to represent a purely ingoing radiation the lower sign must be selected, so that $\Phi_{\hat{l}m\omega}$ becomes asymptotically a function of only $v = t + \tilde{r}_*$ (as well as the regular angular coordinates ϕ_+, θ). We thus find that the correct boundary condition at the horizon is given by

$$\psi_{\hat{l}m\omega}(r_* \to -\infty) \sim e^{-i\gamma_m r_*}. \tag{30}$$

In passing, we remind the reader that frequency modes with $\omega_m < m\Omega_+$ are *superradiant* (see, e.g., Sec. 4.8.2 of [41]). Since in our case $\omega_m = m\Omega_\phi$, this condition translates to $\Omega_\phi < \Omega_+$ [cf. Eq. (55) below] and, using Eqs. (4) and (28), also to $r_0 > r_0^{\rm sr}(a)$, where $a > 0$ and

$$r_0^{\rm sr}(a) \equiv M\left(\frac{r_+^2}{aM}\right)^{2/3}. \tag{31}$$

Hence, for prograde circular geodesic orbits with radius greater than $r_0^{\rm sr}(a)$, all m modes of the scalar field are superradiant. We will demonstrate this behavior numerically in Sec. V B below.

III. SELF-FORCE VIA MODE-SUM REGULARIZATION

In the standard mode-sum scheme [14,30] each vectorial component of the SSF is constructed from regularized *spherical*-harmonic contributions, even in the Kerr case. One starts by defining the full force as the field

$$F_\alpha^{\rm full}(x) \equiv q\nabla_\alpha\Phi(x) = \sum_l F_\alpha^{({\rm full})l}(x), \tag{32}$$

where $F_\alpha^{({\rm full})l}$ denotes the total contribution to $\nabla_\alpha\Phi$ from its spherical-harmonic l mode (summed over m), and x is shorthand for x^μ, an arbitrary field point in the neighborhood of the particle. Each mode $F_\alpha^{({\rm full})l}$ is finite at the particle's location, although, in general, the sided limits $r \to r_0^\pm$ yield two different values, denoted $F_{\alpha\pm}^{({\rm full})l}$, respectively. The SSF is then obtained using the mode-by-mode regularization formula

$$F_\alpha^{\rm self} = \sum_{l=0}^{\infty}(F_{\alpha\pm}^{({\rm full})l} - A_{\alpha\pm}L - B_\alpha) \equiv \sum_{l=0}^{\infty} F_\alpha^{l({\rm reg})}, \tag{33}$$

where $L \equiv l + 1/2$ and the regularized contributions $F_\alpha^{l({\rm reg})}$ no longer exhibit the $\pm$ ambiguity. The (l-independent) *regularization parameters* A_α and B_α were first derived for generic orbits about a Schwarzschild black hole [42] and later also for generic orbits about a Kerr black hole [30]. In the circular-equatorial orbit case considered here, we have $A_{t\pm} = B_t = 0$, and one can show that the mode sum over $F_t^{l({\rm reg})}$ converges exponentially fast [2]. For $\alpha = r$ the regularization parameters are generally nonzero and take a rather complicated form; we give these parameters explicitly in Appendix B (specializing to circular-equatorial orbits). One usually has $F_r^{l({\rm reg})} \propto l^{-2}$, so the mode sum in Eq. (33) converges only as $\sim 1/l$. Recall that one can spare the explicit computation of the ϕ component $F_\phi^{\rm self}$ by using Eq. (6). Also, from symmetry one obviously has $F_\theta^{\rm self} = 0$ identically.

In Kerr spacetime, as we have seen, the scalar field naturally decomposes into spheroidal-harmonic modes, and hence in order to use the mode-sum scheme in its standard form, we must have a preparatory step where the required spherical-harmonic modes $F_{\alpha\pm}^{({\rm full})l}$ are to be constructed out of the spheroidal-harmonic modes of the scalar field. To achieve this, we first consider the formal expansion of the spheroidal harmonics (with given ω) as a series of spherical harmonics,

$$S_{\hat{l}m}(\theta; -a^2\omega_m^2)e^{im\phi} = \sum_{l=0}^{\infty} b_{lm}^{\hat{l}} Y_{lm}(\theta, \phi), \tag{34}$$

where the coupling coefficients $b_{\hat{l}m}^l = b_{lm}^{\hat{l}}(a^2\omega_m^2)$ are determined as prescribed in Appendix A [this expansion is similar to that applied by Hughes in Ref. [34] (with a

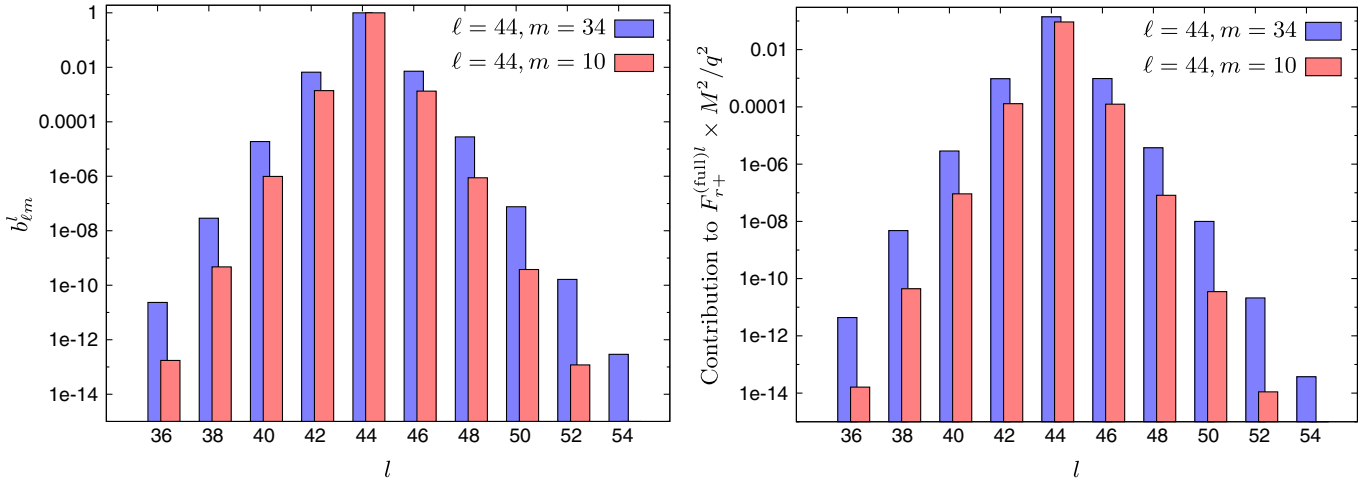

FIG. 1 (color online). Coupling of spheroidal and spherical modes, illustrated here for $a = 0.9M$ and $r_0 = 4M$. Shown are the contributions from a given $\hat{l}$ mode to $b^{\hat{l}}_{lm}$ (left panel) and $F^{(\mathrm{full})l}_{r+}$ (right panel), for various spherical-harmonic l modes. (Note that $b^{\hat{l}}_{lm} = 0$ identically for odd values of $l - \hat{l}$.) The width of the l distribution depends mainly on the magnitude of the spheroidicity parameter, $|\sigma^2| = a^2\omega^2 = a^2m^2\Omega^2_\phi$; the two cases shown, $(\hat{l}, m) = (44, 34)$ and $(\hat{l}, m) = (44, 10)$, have spheroidicities $\sigma^2 = -11.821$ and -1.022, respectively. The point of this illustration is to note that, in practice, one only needs to calculate a handful more spheroidal $\hat{l}$ modes than the desired maximum spherical l mode, especially for smaller a and/or larger r_0, where the coupling is weaker than demonstrated above.

correction noted by Dolan [43])]. Note that the spheroidal harmonics and the spherical harmonics have the same ϕ dependence (i.e., $e^{im\phi}$), and hence only the l modes couple while the m modes do not. Using Eq. (9) in combination with Eqs. (16) and (34) we can then express each of the spherical-harmonic l-mode contributions in Eq. (32) (for $\alpha = t, r$) in the form

$$F^{(\mathrm{full})l}_\alpha(x) = q\nabla_\alpha \sum_{\hat{l}=0}^{\infty} \sum_{m=-\hat{l}}^{\hat{l}} b^{\hat{l}}_{lm}\psi_{\hat{l}m}(r)Y_{lm}(\theta, \phi)e^{-i\omega_m t}/r. \tag{35}$$

The quantities $F^{(\mathrm{full})l}_{\alpha\pm}$ needed as input for the mode-sum formula (33) are obtained from the field $F^{(\mathrm{full})l}_\alpha(x)$ by taking the limits $\theta \to \theta_p$, $\phi \to \phi_p$, and $t \to t_p$, followed by $r \to r^\pm_p$.

Note in Eq. (35) that while formally one must sum over all $\hat{l}$ to construct $F^{(\mathrm{full})l}_\alpha$, in practice this is not necessary as the $\hat{l}$ spectrum (for given l, m) is strongly peaked around $\hat{l} = l$; we demonstrate this behavior in Fig. 1. The bandwidth of $\hat{l}$ around l increases slowly with increasing spheroidicity $|\sigma^2| = a^2\omega^2$, yet even at the largest spheroidicity considered in this work ($\sigma^2 \sim -126$ for $a = 0.998M$, $r_0 = 2M$), we find that only modes within $l - 11 \lesssim \hat{l} \lesssim l + 11$ carry significant contributions to each of the l modes $F^{(\mathrm{full})l}_\alpha$.

IV. NUMERICAL IMPLEMENTATION

For general $\hat{l}$ and m the radial equation (20) has no known analytic solutions so it must be solved numerically. To reduce the computation burden one first notes that the individual $\hat{l}m$ modes of the scalar field are invariant under $m \to -m$ combined with complex conjugation. Consequently, when solving the radial equation we need only calculate the modes that have $m \geq 0$, as we can recover the negative m modes by taking the complex conjugate of the corresponding positive m modes.

A. Boundary conditions and junction conditions

The main numerical task is to solve the inhomogeneous radial equation (20) with the physical boundary conditions described by (27) and (30). The form of the inner boundary conditions makes it more natural to adopt r_* as the coordinate for the numerical integration. Our numerical domain extends from $r_* = r_{*\mathrm{in}} \ll -M$ out to $r_* = r_{*\mathrm{out}} \gg M$ (how these boundaries are chosen in practice will be discussed below). We assume that the radial field $\psi_{\hat{l}m}$ admits an asymptotic expansion in $1/r$ at $r \to \infty$ and an asymptotic expansion in $r - r_+$ at $r \to r_+$. Recalling the leading-order behavior of the physical solutions, expressed in Eqs. (27) and (30), we thus write

$$\psi_{\hat{l}m}(r_{\mathrm{out}}) = e^{+i\omega_m r_{*\mathrm{out}}} \sum_{k=0}^{\bar{k}_{\mathrm{out}}} c^\infty_k r^{-k}_{\mathrm{out}}, \tag{36}$$

$$\psi_{\hat{l}m}(r_{\mathrm{in}}) = e^{-i\gamma_m r_{*\mathrm{in}}} \sum_{k=0}^{\bar{k}_{\mathrm{in}}} c^{eh}_k (r_{\mathrm{in}} - r_+)^k, \tag{37}$$

where $r_{\mathrm{in}} = r(r_{*\mathrm{in}})$, $r_{\mathrm{out}} = r(r_{*\mathrm{out}})$ and the truncation parameters $\bar{k}_{\mathrm{in,out}}$ are chosen such that the boundary conditions reach a prescribed accuracy (see discussion below).

The expansion coefficients are determined by substituting each of the above series into the radial equation. This gives recursion relations for the coefficients $c^{\infty,eh}_{k>0}$, respectively, in terms of $c^{\infty,eh}_0$. These relations are rather unwieldy so we relegate their explicit forms to Appendix C.

The homogeneous solutions obtained with the above boundary conditions (36) and (37) are proportional to the yet-to-be-specified constants c^{∞}_0 and c^{eh}_0, respectively. These constants are determined by imposing suitable matching conditions at the location of the particle. The inhomogeneous solution can be written in the form

$$\psi_{\hat{l}m}(r) = \psi^{-}_{\hat{l}m}(r)\Theta(r_0 - r) + \psi^{+}_{\hat{l}m}(r)\Theta(r - r_0), \quad (38)$$

where $\Theta(x)$ is the Heaviside step function. Substituting this into the radial equation (20) and comparing the coefficients of the delta function and its derivative, we find

$$(\psi^{+}_{\hat{l}m} - \psi^{-}_{\hat{l}m})|_{r_0} = 0, \quad (39)$$

$$(\psi^{+\prime}_{\hat{l}m} - \psi^{-\prime}_{\hat{l}m})|_{r_0} = -\frac{4\pi q r_0}{u^t \Delta_0} S_{\hat{l}m}(\pi/2; -a^2\omega_m^2) \equiv \alpha_{\hat{l}m}, \quad (40)$$

where a prime denotes d/dr and, recall, $\Delta_0 = \Delta(r_0)$. The first equation implies that the field is continuous at the particle, while the second describes the nature of the discontinuity in the field's derivative arising from the delta-function source.

In order to determine the correct values of c^{∞}_0 of c^{eh}_0, for which the conditions (39) and (40) are satisfied, we first numerically solve the radial equation (i) starting from the boundary $r_{\rm out}$ with $c^{\infty}_0 = 1$ and integrating inward, and (ii) starting from the boundary $r_{\rm in}$ with $c^{eh}_0 = 1$ and integrating outward. We denote the two corresponding homogeneous solutions by $\tilde{\psi}^{+}_{\hat{l}m}(r)$ and $\tilde{\psi}^{-}_{\hat{l}m}(r)$, respectively, so

$$\psi^{+}_{\hat{l}m} = c^{\infty}_0 \tilde{\psi}^{+}_{\hat{l}m} \quad \text{and} \quad \psi^{-}_{\hat{l}m} = c^{eh}_0 \tilde{\psi}^{-}_{\hat{l}m}. \quad (41)$$

Substituting these relations in Eqs. (39) and (40) yields two algebraic equations for c^{∞}_0 and c^{eh}_0, whose solutions read

$$c^{eh}_0 = \alpha_{\hat{l}m}\left[\frac{\tilde{\psi}^{+}_{\hat{l}m}(r_0)}{\tilde{\psi}^{-}_{\hat{l}m}(r_0)\tilde{\psi}^{+\prime}_{\hat{l}m}(r_0) - \tilde{\psi}^{+}_{\hat{l}m}(r_0)\tilde{\psi}^{-\prime}_{\hat{l}m}(r_0)}\right], \quad (42)$$

$$c^{\infty}_0 = c^{eh}_0 \frac{\tilde{\psi}^{-}_{\hat{l}m}(r_0)}{\tilde{\psi}^{+}_{\hat{l}m}(r_0)}. \quad (43)$$

Once the coefficients $c^{\infty,eh}_0$ have been determined, the (unique) physical solution is constructed using Eq. (38) with (41).

B. Algorithm

Following is a summary of the numerical procedure we implement for constructing the SSF. We outline the major steps and give some details about the numerical method and the choice of numerical parameters.

(i) Fix a black hole spin a and orbit radius r_0 and calculate the orbital parameters $\mathcal{E}$, $\mathcal{L}$, and Ω_ϕ [Eqs. (2) and (4)], the spherical-harmonic decomposition coefficients $b^{l}_{\hat{l}m}$, and the spheroidal-harmonic eigenvalues $\lambda_{\hat{l}m}$ (the latter two using the method outlined in Appendix A) for all $\hat{l}$ and m in the range $0 \le \hat{l} \le \hat{l}_{\rm max}$, $0 \le m \le \hat{l}$. In this work we typically take $\hat{l}_{\rm max} = 55$, which is sufficient for calculating all spherical-harmonic contributions $F^{({\rm full})l}_{\alpha\pm}$ up to $l \sim 50$ in most cases; see below. (The estimation of the contribution to the mode sum from the remaining large-l tail will be discussed in the next subsection.)

(ii) For each $\hat{l}$ mode, obtain the axially symmetric mode of the radial variable, $\psi_{\hat{l},m=0}$, using the analytic formula (22).

(iii) (For each $m \neq 0$ mode) obtain the boundary conditions for the radial variable using Eqs. (36) and (37), setting $c^{\infty,eh}_k = 1$. Through experimentation we found it practical to set the inner boundary at $r_{*\rm in} = -60M$. The location of the outer boundary required some adjustment depending on the radius of the particle's orbit. In practice we took $r_{*\rm out} = 9000M$ for $r_0 < 30M$ and steadily moved it outward for increasing r_0 in order to achieve sufficiently fast convergence of the asymptotic series (36). The largest value for $r_{*\rm out}$ we used was for $r_0 \ge 100M$ where we had to set $r_{*\rm out} = 6.0 \times 10^4 M$. We chose $\bar{k}_{\rm in,out}$ such that the magnitude of the $\bar{k}_{\rm in,out} + 1$ term drops below a certain threshold, which we set to 10^{-14}.

(iv) (For each $m \neq 0$ mode) integrate the homogeneous part of the radial equation (20) numerically to obtain $\tilde{\psi}^{\pm}_{\hat{l}m}(r)$. For this we used the standard Runge-Kutta Prince-Dormand (8,9) method from the GNU Scientific Library (GSL) [44]. The GSL Runge-Kutta routine allows one to set a global fractional accuracy target, which we took here as 10^{-12}. To test the integrator we used it to solve for a few $m = 0$ modes and compared with the analytic solution (22). We made further use of the GSL to calculate many of the special functions (Legendre polynomials, elliptic integrals, Clebsch-Gordan coefficients, etc.) that our code requires.

(v) Given the numerical solutions $\tilde{\psi}^{\pm}_{\hat{l}m}$ (for each $m \neq 0$ mode), proceed to determine the matching coefficients $c^{\infty,eh}_0$ via Eqs. (42) and (43), and construct the physical inhomogeneous solutions $\psi_{\hat{l}m}$ using Eqs. (38) and (41). Record the values of $\psi_{\hat{l}m}$ and its (one-sided) r and t derivatives at the radius of the particle.

(vi) Given $\psi_{\hat{l}m}(r_0)$ and $\nabla_{\alpha\pm}\psi_{\hat{l}m}(r_0)$ for all spheroidal $\hat{l}m$ modes up to $\hat{l}_{\rm max}$, use Eq. (35) to construct the spherical-harmonic l modes of the full force at the

location of the particle, $F^{(\mathrm{full})l}_{\alpha\pm}$. This procedure allows us to obtain all l modes which do not have significant contributions (through coupling) from the uncalculated modes $\hat{l} > \hat{l}_{\max}$. The highest such l mode, denoted $l_{\max}$, is determined by calculating the contributions from the $\hat{l}_{\max}+1$ spheroidal mode to the various l modes $F^{(\mathrm{full})l}_{\alpha\pm}$, and identifying the highest value of l for which this contribution falls below a given threshold, set here to 10^{-12} (fractionally). With $\hat{l}_{\max} = 55$ we find $l_{\max} \geq 44$ for all a, r_0 within the parameter range considered in this work (lower values of $l_{\max}$ for larger $|a|$ and smaller r_0, with typical values around $l_{\max} \sim 50$); cf. Figure 1.

(vii) In the final step, calculate the regularized modes $F^{l(\mathrm{reg})}_{\alpha}$ defined in Eq. (33) using the regularization parameters given in Appendix B. Then sum over l modes as in Eq. (33) to obtain the desired SSF. Formally, the mode-sum formula (33) requires summation over all l modes from $l = 0$ to $l = \infty$. In practice, of course, this is neither possible nor necessary. For the t component, the mode sum converges exponentially fast, and we typically find that the contribution from the modes $l \gtrsim 15$ can be safely neglected. For the radial component the situation is a little more subtle, as the mode sum converges only as $\sim 1/l$ in this case—artificially truncating the series at $l \sim 50$ may potentially result in an error of as much as a few tens of percent in the final SSF. It is therefore important to estimate the contribution from the $l > l_{\max}$ tail of the mode sum. The method we used for this estimation follows that of Barack and Sago [21], and for completeness we review it in the next subsection.

C. Estimation of the high-l tail contribution

We write the total radial component of the SSF as a sum of two pieces, a numerically computed piece and a large-l tail:

$$F^{\mathrm{self}}_r = F^{l\leq l_{\max}}_r + F^{l>l_{\max}}_r, \tag{44}$$

where, with $F^{l(\mathrm{reg})}_r$ as defined in Eq. (33),

$$F^{l\leq l_{\max}}_r \equiv \sum_{l=0}^{l_{\max}} F^{l(\mathrm{reg})}_r \quad \text{and} \quad F^{l>l_{\max}}_r \equiv \sum_{l=l_{\max}+1}^{\infty} F^{l(\mathrm{reg})}_r. \tag{45}$$

To evaluate the large-l tail $F^r_{l>l_{\max}}$ we extrapolate the last $\bar{n}$ numerically calculated l modes using the fitting formula

$$F^{l(\mathrm{reg})}_r \simeq \sum_{n=1}^{N} \frac{D^r_{2n}}{L^{2n}}, \tag{46}$$

where, recall, $L = l + 1/2$ (how we chose $\bar{n}$ and N in practice is discussed below). For this fitting we used a standard least-squares algorithm from the GSL. Given the coefficients D^r_{2n}, we then estimate the high-l contribution using the formula

$$\begin{aligned} F^{l>l_{\max}}_r &\simeq \sum_{n=1}^{N} D^r_{2n} \sum_{l=l_{\max}+1}^{\infty} L^{-2n} \\ &= \sum_{n=1}^{N} \frac{D^r_{2n}}{(2n-1)!} \Psi_{2n-1}(l_{\max} + 3/2), \end{aligned} \tag{47}$$

where $\Psi_n(x)$ is the polygamma function of order n defined as

$$\Psi_n(x) = \frac{d^{n+1}[\log\Gamma(x)]}{dx^{n+1}}, \tag{48}$$

with $\Gamma(x)$ being the standard gamma function.

Practical use of this estimation method requires some experimentation. For a given $N \in \{3, 4, 5\}$ we considered a weighted average of the values obtained for F^{self}_r as we vary $\bar{n}$ from 20 to 35, where the weighting for each term is given by the square of the inverse of the fractional difference in the value of F^{self}_r as we increase $\bar{n}$ by 1 (this procedure is meant to bias the average in favor of $\bar{n}$ values for which F^{self}_r depends only weakly on the number of fitting modes.) We obtain three different average values corresponding to $N = 3, 4, 5$, and use the variance of these values to estimate our numerical accuracy (we record as significant figures only those figures that remain fixed as we vary N). This error dominates the overall error budget of the SSF, and we hence use it to estimate to overall accuracy of our final SSF results.

It should be noted that the relative contribution from the large-l tail is particularly important in the scalar-field case (as compared with the gravitational case). This is because the contribution from the first few l modes turns out to be relatively large and opposite in sign with respect to that of the higher modes. In the Schwarzschild case, the contributions from the $l = 0$, 1 modes are both negative and (e.g., for $r_0 = 6M$) conspire to nearly cancel out the combined contributions from $l = 3$–6. In the Kerr case this cancellation sometimes involves an even greater number of modes (particularly near a, r_0 values for which the radial SSF vanishes—see below). This behavior is not observed in the gravitational case [21]—at least not for the Lorenz-gauge GSF in the Schwarzschild case.

V. CODE VALIDATION AND RESULTS

A. High-l behavior

According to mode-sum theory [14], the regularized modes $F^{l(\mathrm{reg})}_r$ in the mode-sum formula (33) should fall off as $\sim 1/l^2$ for large l. This behavior relies sensitively on the delicate cancellation of as many as three leading terms in the $1/l$ expansion of the full modes $F^{(\mathrm{full})l}_{r\pm}$ (which itself diverges at $\sim l$), and hence provides an excellent test of validity for our numerical results. Indeed, we have been able to confirm a clear $\sim 1/l^2$ behavior in our numerical data—an example is presented in Fig. 2. Similarly for the

time component, we know from theory that the regularized contributions $F_t^{l(\mathrm{reg})}$ decay exponentially with l, and again we were able to observe this behavior in our numerical data—see again Fig. 2 for an illustration. The above two tests give us confidence that the high-$\hat{l}$ spheroidal contributions (whose numerical computation is most demanding) are calculated correctly, and that the spherical-harmonic decomposition procedure is implemented properly. These tests also confirm, for the first time, the validity of the regularization parameters in the Kerr case (for circular-equatorial orbits).

B. Energy flux in the scalar waves

The above validity check only tests the high-l output of our code. We now discuss a second, more quantitative test, which probes primarily the lower-l portion of the mode sum (and in that sense it is complementary to the first test). From global energy conservation we have that the work done by the dissipative piece (here the t component) of the SSF must be balanced by the flux of energy carried away in scalar-field radiation. We can use our code to compute the flux of energy radiated to infinity and down the black hole, and the result must be consistent with the value of the local dissipative SSF. For the t component the mode sum converges exponentially fast, and it is for this reason we argued that the energy-balance test is mostly sensitive to the low-l portion of the mode sum.

We first briefly review the relevant formalism for computing the radiative flux. The stress-energy tensor of the scalar field is given by

$$T_{\alpha\beta} = \frac{1}{4\pi}\left(\Phi_{,\alpha}\Phi_{,\beta} - \frac{1}{2}g_{\alpha\beta}\Phi^{,\mu}\Phi_{,\mu}\right), \tag{49}$$

where, as always, $g_{\alpha\beta}$ denotes the Kerr background metric. We wish to consider the flux of scalar-field energy flowing to infinity and down the hole. Let Σ^+ and Σ^- represent two (timelike) hypersurfaces with $r = \mathrm{const} \gg M$ and $r_* = \mathrm{const} \ll -M$, respectively; and let $d\Sigma^\pm$ represent a portion of $\Sigma^\pm$ of a small time span dt. The amount of scalar-field energy flowing through $\Sigma^\pm$ over time dt is expressed by

$$dE_\pm = \mp \oint T^\alpha_\beta \xi^\beta_{(t)} d\Sigma^\pm_\alpha \tag{50}$$

(see, e.g., Sec. 4.3.6 of [39]), where $d\Sigma^\pm_\alpha$ represent outward-pointing surface elements on $d\Sigma^\pm$, and the integral is performed over the corresponding two-spheres of constant r, t. The signs are chosen such that the *outflow* of energy through Σ^+ is positive, and so is the *inflow* of energy through Σ^- in the Schwarzschild case (recall, however, that dE_- can turn negative in the Kerr case, when superradiance is manifest). In coordinate form we have $\xi^\beta_{(t)} = \delta^\beta_t$ and $d\Sigma^\pm_\alpha = (-g^{(3)})^{1/2}\hat{r}_\alpha d\theta d\phi dt = \delta^r_\alpha \rho^2 \sin\theta d\theta d\phi dt$, where $g^{(3)} = -\Delta\rho^2\sin^2\theta$ is the determinant of the induced metric on $\Sigma^\pm$, and $\hat{r}_\alpha = \delta^r_\alpha (g^{rr})^{-1/2} = \delta^r_\alpha \Delta^{-1/2}\rho$ is an outward-pointing radial vector of a unit length. The (time-independent) flux of energy through $\Sigma_\pm$ is hence given by

$$\dot{E}_\pm \equiv \frac{dE_\pm}{dt} = \mp\Delta \oint T_{tr} d\Omega. \tag{51}$$

From Eq. (49) we have $T_{tr} = (4\pi)^{-1}\Phi_{,t}\Phi_{,r}$, which, in order to facilitate the angular integration in Eq. (51), we write as $T_{tr} = (4\pi)^{-1}\Phi_{,t}\Phi^*_{,r}$, with an asterisk denoting complex conjugation (this is allowed since Φ is a real field). We then substitute the spheroidal-harmonic decom-

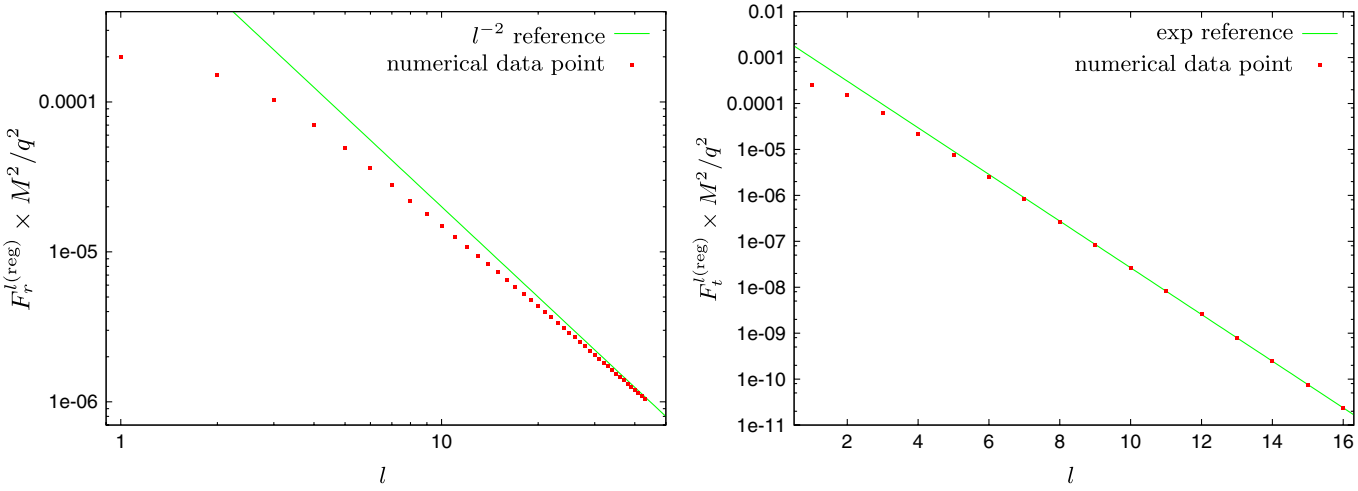

FIG. 2 (color online). *Left panel:* The regularized modes $F_r^{l(\mathrm{reg})}$ as a function of l for $r_0 = 5M$ and $a = 0.5M$. The solid reference line is $\propto 1/l^2$. The regularized modes demonstrate an asymptotic $\propto 1/l^2$ behavior at large l, as expected from theory (note the log-log scale). *Right panel:* The regularized modes $F_t^{l(\mathrm{reg})}$ as a function of l for $r_0 = 5M$ and $a = 0.8M$. The solid reference line is exponentially decreasing with l. The regularized modes of the t component show a clear exponential decay at large l, as expected from theory (note the semilog scale). Similar behavior is observed for other values of r_0 and a.

position

$$\Phi = \frac{1}{r}\sum_{\hat{l}m}\psi_{\hat{l}m}(r)S_{\hat{l}m}(\theta;-a^2\omega_m^2)e^{im\phi}e^{-i\omega_m t} \equiv \sum_{\hat{l}m}\Phi_{\hat{l}m}, \tag{52}$$

making the replacement $(\Phi_{\hat{l}m})_{,t} = -i\omega_m\Phi_{\hat{l}m}$. The asymptotic relations

$$\begin{aligned}\psi_{\hat{l}m}(r\to\infty) &= c_0^{\infty}\exp(i\omega_m r),\\ \psi_{\hat{l}m}(r\to r_+) &= c_0^{eh}\exp(-i\gamma_m r_*)\end{aligned} \tag{53}$$

[recall Eqs. (36) and (37)] also allow us to replace $(\Phi^*_{\hat{l}m})_{,r} = -im\Omega_\phi\Phi^*_{\hat{l}m}$ for $r\to\infty$, and $(\Phi^*_{\hat{l}m})_{,r} = 2iMr_+\Delta^{-1}m(\Omega_\phi-\Omega_+)\Phi^*_{\hat{l}m}$ for $r\to r_+$ [where in the last equality we used Eqs. (17), (26), and (28)]. With these substitutions, the integral in Eq. (51) is readily evaluated using the orthonormality relation (10), giving

$$\dot{E}_+ = \frac{1}{4\pi}\sum_{\hat{l}m} m^2\Omega_\phi^2|c_0^{\infty}|^2, \tag{54}$$

$$\dot{E}_- = \frac{M}{2\pi r_+}\sum_{\hat{l}m} m^2\Omega_\phi(\Omega_\phi-\Omega_+)|c_0^{eh}|^2. \tag{55}$$

In Table I we display numerical values for the total energy flux, $\dot{E}_{\rm total} \equiv \dot{E}_+ + \dot{E}_-$, as computed using our code based on Eqs. (54) and (55). For a similar orbital setup, Gralla *et al.* [32] have previously calculated the total flux of scalar-field *angular-momentum*, $\dot{L}_{\rm total}$. In the case of circular-equatorial orbits the simple relation $\dot{E}_{\rm total} = \Omega_\phi\dot{L}_{\rm total}$ applies, which gives us a direct comparison with the results obtained in Ref. [32]. The data in Table I show good agreement between our fluxes and those of Gralla *et al.*, with relative differences comparable in magnitude to the estimated relative numerical error in the data of Ref. [32].

TABLE I. Scalar-field energy flux for various values of the spin parameter a and orbital radius r_0. The third column displays the total flux of energy radiated to infinity and down the black hole, as extracted from our numerical solutions. The fourth column presents the fraction of the total power absorbed by the black hole, with negative values indicating superradiance. The fifth column compares our fluxes to those obtained by Gralla, Friedman, and Wiseman (GFW) [32], showing a good agreement. (GFW provide results for the radiated angular-momentum, which we convert here to radiated energy using the relation $\dot{E}_{\rm total} = \Omega_\phi\dot{L}_{\rm total}$; their results are given with six significant figures.) In the last column we test our SSF results (for the dissipative component) against the balance relation (57) as discussed in Sec. V C; $\dot{\mathcal{E}}(<0)$ is the rate at which the particle's scalar energy is dissipated, as computed from the local SSF using Eq. (56). In this table (and all subsequent tables) we use an exponential notation whereby (e.g.) "e−3" stands for $\times 10^{-3}$. All decimal places presented are significant.

a/M	r_0/M	$q^{-2}\dot{E}_{\rm total}$	$\dot{E}_-/\dot{E}_{\rm total}$	$1-\dot{E}_{\rm total}/\dot{E}^{\rm GFW}_{\rm total}$	$1-\dot{E}_{\rm total}/\dot{\mathcal{E}}$
0.998	2	4.397 597 9e−3	−0.2486	7.06e−7	−4.7e−10
	4	6.656 188 88e−4	−0.1168	2.12e−7	−1.6e−10
	6	1.697 124 83e−4	−0.0692	1.12e−6	−9.2e−11
	8	6.044 943 14e−5	−0.0464	−2.12e−6	−4.6e−11
	10	2.648 456 08e−5	−0.0337	6.65e−8	−3.7e−11
	20	1.873 887 89e−6	−0.0120		−2.8e−12
	40	1.237 962 12e−7	−0.0041		7.7e−11
0.5	6	2.029 186 08e−4	−0.0248	−5.19e−7	−8.9e−11
	8	6.762 029 50e−5	−0.0196	−1.76e−6	−6.8e−11
	10	2.866 378 38e−5	−0.0151	7.33e−7	−3.3e−11
	20	1.926 050 66e−6	−0.0058		−1.0e−12
	40	1.249 987 16e−7	−0.0021		−3.5e−11
0.0	6	2.551 999 67e−4	0.0308		−9.2e−11
	8	7.725 479 78e−5	0.0114	1.98e−6	−6.2e−11
	10	3.137 665 25e−5	0.0054	1.28e−7	−4.1e−11
	20	1.983 669 95e−6	0.0006		−4.6e−12
	40	1.262 267 16e−7	0.0001		4.2e−11
−0.5	8	9.023 154 46e−5	0.0468	−5.01e−7	−4.9e−11
	10	3.475 796 47e−5	0.0284	5.20e−6	−4.6e−11
	20	2.047 187 63e−6	0.0073		3.4e−12
	40	1.276 004 90e−7	0.0022		5.2e−11
−0.998	9	6.225 602 92e−5	0.0644	−7.86e−7	−5.0e−11
	10	3.888 393 60e−5	0.0519	−1.56e−6	−4.2e−11
	20	2.116 432 77e−6	0.0142		2.2e−11
	40	1.289 925 55e−7	0.0044		−6.1e−11

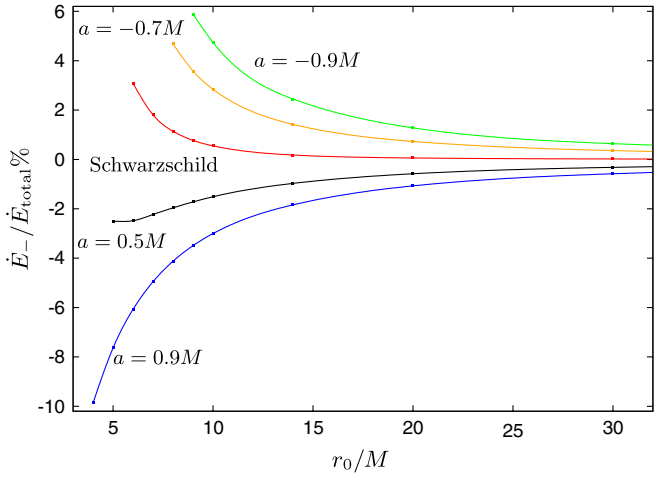

FIG. 3 (color online). The horizon flux of scalar-field energy, $\dot{E}_-$, as a percentage of the total flux for different orbital radii r_0 and spin parameters a. The curves are interpolations based on the numerical data points shown. Superradiance behavior ($\dot{E}_- < 0$) is manifest whenever the horizon's angular velocity Ω_+ is greater than that of the particle.

Table I also displays numerical results for the horizon flux, $\dot{E}_-$, expressed as a fraction of $\dot{E}_{\rm total}$. Superradiance ($\dot{E}_- < 0$) is manifest whenever $\Omega_+ > \Omega_\phi$. Horizon absorption does not normally exceed $\sim 10\%$ even for strong-field orbits (as also noted by Hughes [34] in the gravitational case), but prograde orbits around a fast rotating hole can display extreme superradiance behavior [nearly 25% negative absorption in the example of $(a, r_0) = (0.998M, 2M)$]. The graph in Fig. 3 displays some more horizon absorption data.

C. Dissipative component of the SSF

In the case of circular-equatorial orbits the entire information about the dissipative effect of the SSF is contained in the two components F_t and F_ϕ. Specifically, we obtain from Eq. (1)

$$\mu\dot{\mathcal{E}} = -(u^t)^{-1}F_t, \qquad \mu\dot{\mathcal{L}} = (u^t)^{-1}F_\phi, \tag{56}$$

where, as elsewhere in this work, an overdot denotes d/dt. The relation (6) implies that, in practice, we need only calculate one of the two components F_t and F_ϕ—here we choose to calculate the former. Sample numerical data for F_t are presented in Table II.

In our stationary setting, the rate at which the particle is losing scalar energy, given by $-\dot{\mathcal{E}}$, must equal the rate at which energy flows to infinity and down the black hole, given by $\dot{E}_{\rm total}$. Using Eq. (56) we may express this energy-balance relation directly in terms of the SSF:

$$F_t = -\mu u^t \dot{\mathcal{E}} = \mu u^t \dot{E}_{\rm total}. \tag{57}$$

As discussed above, this allows us to test our computation of F_t (primarily the low-l portion of the mode sum) by verifying that our numerical results satisfy Eq. (57). As the data presented in the rightmost column of Table I demonstrate, we indeed find a very good agreement.

It is also interesting to test our results against the weak-field/slow-motion analytic formula derived by Gal'tsov [33],

$$F_t^{\rm Gal'tsov} = \frac{1}{3}q^2\Omega_\phi\left(r_0^2\Omega_\phi^3 + \frac{2M^3 r_+}{r_0^4}(\Omega_\phi - \Omega_+)\right), \tag{58}$$

which is valid for $r_0 \gg M$. Here the first term corresponds to the radiation heading out to infinity and the second to the radiation absorbed by the black hole. In Fig. 4 we plot the relative difference between the "full" SSF computed here and $F_t^{\rm Gal'tsov}$ as a function of r_0 for a couple of a values (we choose the two extreme cases $a = \pm 0.998M$). Our results seem to obey Gal'tsov's formula for large orbital radii, as expected.

TABLE II. Sample numerical results for the t component of the SSF. Entries left empty correspond to orbits below the innermost stable circular orbit (ISCO). All figures presented are significant.

	$(M^2/q^2)F_t$						
r_0/M	$a = -0.9M$	$a = -0.7M$	$a = -0.5M$	$a = 0$	$a = 0.5M$	$a = 0.7M$	$a = 0.9M$
4						1.359 218 15e−3	1.142 048 20e−3
5					6.076 840 87e−4	5.357 685 61e−4	4.796 349 85e−4
6				3.609 072 54e−4	2.783 947 98e−4	2.551 610 13e−4	2.357 338 53e−4
7				1.767 320 19e−4	1.463 664 47e−4	1.371 037 03e−4	1.290 467 47e−4
8			1.157 813 60e−4	9.772 044 85e−5	8.448 763 16e−5	8.024 073 93e−5	7.645 191 60e−5
10	4.604 751 73e−5	4.385 905 19e−5	4.184 290 73e−5	3.750 227 27e−5	3.404 105 32e−5	3.286 111 97e−5	3.177 601 68e−5
14	1.031 739 65e−5	1.005 390 90e−5	9.803 874 38e−6	9.236 726 60e−6	8.747 282 07e−6	8.570 772 24e−6	8.403 735 78e−6
20	2.284 571 08e−6	2.253 115 11e−6	2.222 740 47e−6	2.151 592 16e−6	2.087 092 37e−6	2.063 009 02e−6	2.039 805 74e−6
30	4.307 612 67e−7	4.277 292 35e−7	4.247 675 92e−7	4.176 785 76e−7	4.110 356 02e−7	4.084 969 12e−7	4.060 210 07e−7
50	5.434 198 39e−8	5.417 293 02e−8	5.400 643 64e−8	5.360 166 21e−8	5.321 327 22e−8	5.306 236 47e−8	5.291 388 07e−8
70	1.402 568 23e−8	1.399 991 78e−8	1.397 445 75e−8	1.391 216 44e−8	1.385 181 65e−8	1.382 821 03e−8	1.380 489 82e−8
100	3.350 722 95e−9	3.347 179 63e−9	3.343 669 14e−9	3.335 038 95e−9	3.326 618 12e−9	3.323 307 55e−9	3.320 029 17e−9

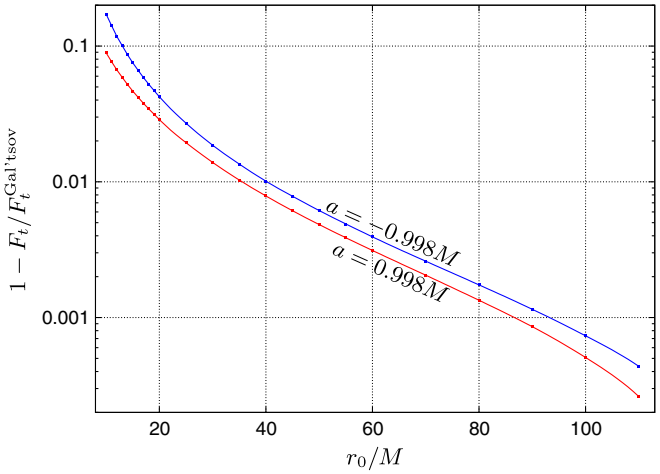

FIG. 4 (color online). Time component of the SSF: comparison with Gal'tsov's slow-motion formula. Plotted is the relative difference between our full SSF F_t and Gal'tsov's weak-field/slow-motion analytic approximation (58) as a function of orbital radius r_0. Solid lines are interpolations of the data points shown. We show results for $a = \pm 0.998M$; similar agreement between F_t and $F_t^{\mathrm{Gal'tsov}}$ at large r_0 is manifest for other values of a, too.

Lastly, we note that our value of F_t for $(a, r_0) = (0, 6M)$ (see Table II) coincides through all nine significant figures with the value computed by Haas and Poisson in Ref. [45].

D. Conservative component of the SSF

In our orbital setting, the conservative effect of the SSF is entirely accounted for by its radial component F_r. The computation of this component is more involved, as in this case the mode sum requires regularization, and (relatedly) the mode-sum series exhibits slow convergence. While results for the dissipative SSF for circular-equatorial orbits about a Kerr black hole (obtained indirectly from the asymptotic fluxes) already exist in the literature, our results for F_r are new.

Table III presents F_r data obtained for a range of a and r_0 values. Our results for the Schwarzschild case ($a = 0$) agree with those of Diaz-Rivera *et al.* [17] through all significant figures. The most striking feature of our results is that—unlike in the Schwarzschild case where the radial SSF is always repulsive (outward pointing)—here we find that for certain prograde orbits, F_r becomes *attractive* (inward pointing). This behavior is better illustrated in Fig. 5, where we present a contour plot of F_r across the parameter space of a, r_0. This plot is based on the data shown in Table III as well as many other intermediate data points. A few fixed-r_0 and fixed-a cross sections of the contour plot are presented in Fig. 6 for clarity.

We observe the following: (i) For retrograde orbits ($a < 0$) the radial SSF is always repulsive, as in the Schwarzschild case. (ii) For prograde orbits ($a > 0$) there exists an a-dependent radius r_c at which the radial SSF vanishes; it is repulsive for $r_0 < r_c$ and attractive for $r_0 > r_c$. (iii) The critical radius r_c *decreases* monotonically with increasing a. (iv) The critical orbit coincides with the ISCO for $a \simeq 0.461M$; hence, all stable circular geodesics experience an attractive radial SSF when $a \gtrsim 0.461M$. It is interesting to note that Burko [16] observed a similar change of sign in the radial SSF when studying accelerated (nongeodesic) circular orbits in Schwarzschild geometry.

To gain some intuition about the above behavior of the radial SSF, it is instructive to analyze our results in the context of PN theory. In the Schwarzschild case, a weak-field expression for the radial SSF was worked out to high PN order by Hikida *et al.* in Ref. [46]. Only the leading 3PN and 4PN terms are given explicitly in that work. They read [49]

TABLE III. Sample numerical results for the r component of the SSF. Entries left empty correspond to orbits below the ISCO. All figures presented are significant. The numerical accuracy is lower compared to that of F_t as a result of (i) the regularization procedure involved in obtaining F_r, and (ii) the slow decay of the large-l tail in the case of F_r (compared with the exponential decay of the tail for F_t).

	$(M^2/q^2)F_r$						
r_0/M	$a = -0.9M$	$a = -0.7M$	$a = -0.5M$	$a = 0$	$a = 0.5M$	$a = 0.7M$	$a = 0.9M$
4						−5.241 94e−4	−9.5941e−4
5					−4.160 235e−5	−2.044 174e−4	−3.634 48e−4
6				1.677 283e−4	−2.421 685e−5	−9.528 095e−5	−1.645 525e−4
7				7.850 679e−5	−1.467 677e−5	−4.980 678e−5	−8.410 331e−5
8			9.642 777e−5	4.082 502e−5	−9.219 07e−6	−2.829 488e−5	−4.696 081e−5
10	4.939 995e−5	4.100 712e−5	3.289 42e−5	1.378 448e−5	−4.035 17e−6	−1.091 819e−5	−1.768 232e−5
14	9.968 208e−6	8.303 689e−6	6.670 43e−6	2.720 083e−6	−1.075 73e−6	−2.561 183e−6	−4.029 35e−6
20	1.878 548e−6	1.565 128e−6	1.255 001 9e−6	4.937 90e−7	−2.502 60e−7	−5.439 42e−7	−8.354 74e−7
30	2.873 310e−7	2.389 538e−7	1.908 43e−7	7.1719e−8	−4.595 209e−8	−9.266 82e−8	−1.391 883e−7
50	2.743 58e−8	2.272 902e−8	1.803 392e−8	6.3467e−9	−5.274 19e−9	−9.905 89e−9	−1.452 810e−8
70	5.875 43e−9	4.8525e−9	3.8312e−9	1.2845e−9	−1.253 52e−9	−2.266 49e−9	−3.278 20e−9
100	1.1508e−9	9.4715e−10	7.4364e−10	2.356e−10	−2.7134e−10	−4.7388e−10	−6.7625e−10

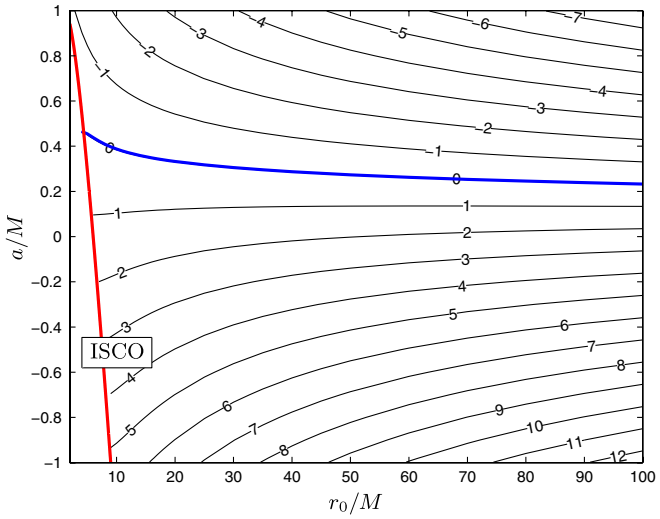

FIG. 5 (color online). The radial component of the SSF, multiplied by r_0^5 for convenience, across the a, r_0 parameter space. Contour lines are lines of fixed $r_0^5 F_r$, with labels giving the value of $(M/q)^2(r_0/M)^5 F_r$. The near-vertical thick line indicates the location of the ISCO, while the near-horizontal thick line marks the curve $r_0 = r_c(a)$ along which the radial SSF vanishes. The two lines intersect at $a \simeq 0.461M$; for $a \gtrsim 0.461M$ all stable circular geodesics experience an attractive radial SSF.

$$F_r^{(a=0)}(r_0 \gg M) = \frac{q^2}{r_0^2}\left[\left(\frac{M}{r_0}\right)^3 [p_3 + p_3^{\log} \ln(r_0/M)] + \left(\frac{M}{r_0}\right)^4 [p_4 + p_4^{\log} \ln(r_0/M)]\right], \quad (59)$$

where the coefficient are given by

$$p_3 = -\frac{4}{3}(\gamma + \ln 2) + \frac{7}{64}\pi^2 - \frac{2}{9} = -0.836\,551\ldots,$$
$$p_3^{\log} = \frac{2}{3},$$
$$p_4 = -\frac{14}{3}\gamma - \frac{66}{5}\ln 2 + \frac{29}{1024}\pi^2 + \frac{604}{45} = 1.858\,52\ldots,$$
$$p_4^{\log} = \frac{7}{3}, \quad (60)$$

with $\gamma = 0.577\,215\ldots$ being the Euler constant. Note the leading 3PN term is dominated by a "logarithmic running" term. Using Eq. (59) as an ansatz for the $a = 0$ case, we performed a two-dimensional fit of a large-r_0 subset of our numerical data to a model of the form $F_r = F_r^{(a=0)} + a\mathcal{L}\times$ power series in M/r_0. We find, at leading order,

$$F_r(r \gg M) = F_r^{(a=0)} + p_3^{\rm so}\frac{q^2 a\mathcal{L}}{r_0^2}\left(\frac{M}{r_0}\right)^3, \quad (61)$$

with

$$p_3^{\rm so} \simeq -1.000\,91. \quad (62)$$

Our numerical accuracy was not sufficient to distinguish between different PN models (including possible logarithmic terms) at higher PN orders, so we do not present here fit results beyond the leading 3PN spin term. This leading term has the interpretation of a spin-orbit coupling ("$\vec{a}\cdot\vec{L}$"). We are not aware of any explicit analytic calculation of this term in the PN literature. (It might be possible to extract the 3PN spin-orbit term from the formal results of Ref. [47], which, however, we have not attempted here.) Our numerical fit suggests that the coefficient $p_3^{\rm so}$ of the leading 3PN spin-orbit term is simply -1.

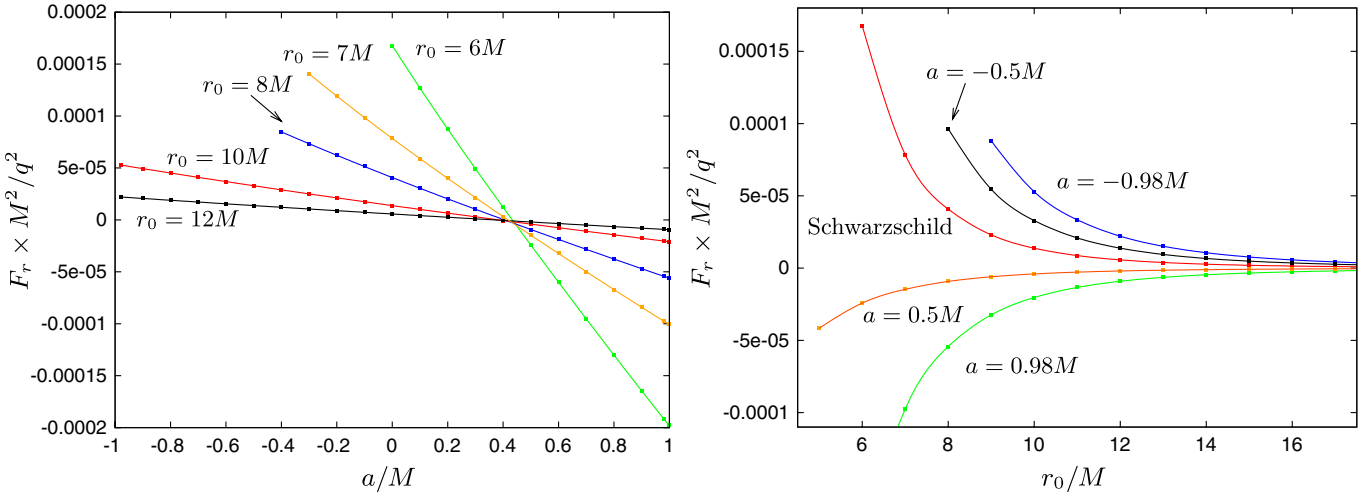

FIG. 6 (color online). *Left panel:* Radial component of the SSF as a function of a for various fixed values of the orbital radius r_0. *Right panel:* Radial component of the SSF as a function of r_0 for various fixed values of the spin parameter a. In both panels dots represent numerical data points, and solid lines are interpolations.

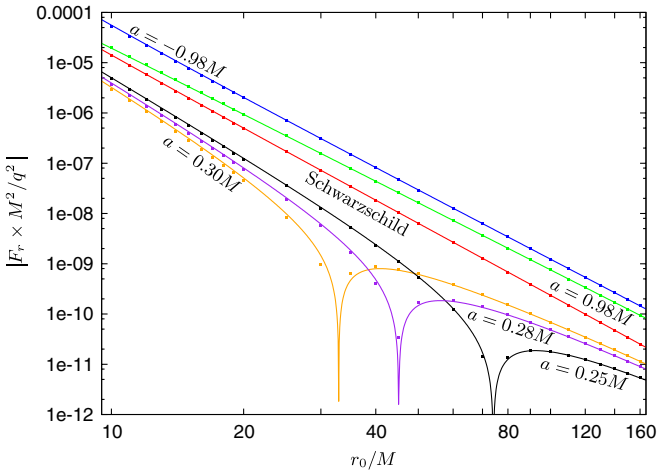

FIG. 7 (color online). Comparison of numerical data for F_r (dots) with the PN fit model (61) (solid lines). For prograde orbits with $a \lesssim 0.461M$ the radial SSF changes sign at $r_0 = r_c(a)$; cf. Figs. 5 and 6.

In Fig. 7 we plot some of our F_r numerical data points against the analytic PN model (61). A good agreement is manifest down to radii as small as $r_0 = 10M$ where the difference between our fitted PN formula (61) and our numerical results is, in all cases, no more than 8%. At $r_0 = 20M$ this difference is never greater than 3%.

We note that $\mathcal{L} \sim r_0^{1/2}$ for large r_0 [recall Eq. (2)], and hence the leading spin term in Eq. (61) dominates the overall behavior of F_r at sufficiently large r_0, falling off as $\sim r_0^{-4.5}$. At intermediate values of r_0, this term, which is negative for $a > 0$, competes with the leading Schwarzschild term, which falls off as $\sim r_0^{-5} \ln r_0$ and is positive. This, we now observe, gives rise to the change of sign observed for F_r in our numerical data.

VI. CONCLUDING REMARKS AND FUTURE WORK

In this work we presented a first calculation of the SSF experienced by a particle orbiting a Kerr black hole, specializing to circular and equatorial geodesic orbits. This represented a first application of the mode-sum method in Kerr spacetime, and as a by-product, we confirmed the analytic values of the regularization parameters A_α, B_α, and C_α, as calculated in [30], for the above class of orbits. Our numerical calculation relied on a standard frequency-domain decomposition of the scalar-field equation in terms of spheroidal harmonics; the spherical-harmonic contributions required within the regularization procedure were obtained by projecting the spheroidal-harmonic contributions onto a basis of spherical harmonics.

We tested the performance of our code in various ways. The contribution to the SSF from the high-l modes was found to possess the expected behavior, falling off exponentially for the time component and as $\sim l^{-2}$ for the radial component. We confirmed numerically that the work done by the time component of the SSF precisely balances the energy in scalar waves radiated out to infinity and down through the event horizon. The energy flux calculated from our code also agreed closely with the previous numerical results by Gralla *et al.* [32] as well as with Galt'sov's analytic formula [33] in the large-r_0 regime. The radial, conservative component of the SSF was calculated here for the first time. Our code produces good agreement with the previous results of Diaz-Rivera *et al.* [17] in the Schwarzschild case. For nonzero spin, we observed a qualitatively new behavior: The radial SSF on prograde orbits with radius larger than a certain a-dependent radius r_c turns from repulsive (as in the Schwarzschild case) to attractive. While we have no genuine physical intuition to explain the direction of the radial SSF (not even in the Schwarzschild case), we observed, at a formal level, that the above change of sign may be attributed to a competition between a repulsive Schwarzschild term and an attractive spin-orbit coupling term.

This observation came from fitting our numerical SSF data to an analytic PN model at large r_0. We thus derived a numerical approximation for the leading-order, 3PN spin-correction term. It would be interesting to test our result against an analytic PN computation of the radial SSF, once the PN result becomes available. To further make contact with PN theory it would be necessary to extract higher-order terms in the PN series, and for this it may be necessary to improve the accuracy of our code at large orbital radii. The main limiting factor, and by far the dominant source of error in our calculation, is the large contribution to the SSF from the long uncomputed tail of the l-mode series. The relative contribution of this tail increases with r_0; in our analysis the uncomputed tail contribution for $r_0 = 100M$ is more than twice that of the computed modes. The problem can be mitigated in future work by pushing our numerical calculation to higher $\hat{l}$, or—better still—by obtaining analytic expressions for some of the higher-order terms in the $1/l$ mode sum, thereby accelerating the convergence of the mode sum. (This latter technique was applied successfully by Detweiler *et al.* in the Schwarzschild case [48].)

As mentioned in the Introduction, in general, a frequency-domain application of the mode-sum method is made difficult by the bad convergence of the frequency mode sum along the particle's orbit ("Gibbs phenomenon"). The problem is unnoticed for circular orbits, since in this case the scalar field is a smooth function of time along the orbit. However, the issue will need to be addressed in contemplating the extension of our code to more generic orbits. The recently introduced method of "extended homogeneous solutions" [31] proposes a simple method to overcome the above difficulty, and we envisage incorporating this method in a future extended version of our code. We have already started work on generalizing the

code to eccentric orbits (which, as a first step, we keep equatorial).

Extension to the gravitational problem is more challenging. The main obstacle is the lack of a formal framework for analyzing Lorenz-gauge metric perturbations in the frequency domain in Kerr spacetime. A potential avenue of approach would be to work with coupled tensorial spherical harmonics, although this may pose a significant technical challenge. Another possibility would be to develop a suitable tensorial spheroidal-harmonic basis for decomposition in Kerr spacetime, akin to the tensorial spherical harmonics that can be used in the Schwarzschild case.

ACKNOWLEDGMENTS

We are grateful to Thibault Damour for crucial advice relating to our PN fit model. We would also like to thank Sarp Akcay, Steven Detweiler, Sam Dolan, Sam Gralla, and Bernard Whiting for helpful comments. N. W.'s work was supported by an STFC grant. L. B. acknowledges additional support from STFC through Grant No. PP/E001025/1.

APPENDIX A: SPHEROIDAL HARMONICS AND THEIR EXPANSION IN SPHERICAL HARMONICS

The spheroidal harmonics $S_{\hat{l}m}(\theta;\sigma^2)e^{im\phi}$ satisfy the differential equation

$$\left[\frac{1}{\sin\theta}\frac{\partial}{\partial\theta}\left(\sin\theta\frac{\partial}{\partial\theta}\right)+\left(\lambda_{\hat{l}m}-\sigma^2\cos^2\theta-\frac{1}{\sin^2\theta}\frac{\partial^2}{\partial\phi^2}\right)\right]S_{\hat{l}m}(\theta;\sigma^2)e^{im\phi}=0, \tag{A1}$$

where the constant parameter σ^2 is the spheroidicity. The functions $S_{\hat{l}m}(\theta;\sigma^2)e^{im\phi}$ are called *oblate* or *prolate* spheroidal harmonics, depending on whether σ^2 is negative or positive, respectively. A useful and efficient method for calculating the spheroidal harmonics is via decomposition in spherical harmonics. This method is doubly useful in our case, as it automatically generates the spherical-harmonic data required as input for the mode-sum formula.

The expansion of a given spheroidal harmonic as a series of spherical harmonics, for given m, takes the form

$$S_{\hat{l}m}(\theta;\sigma^2)e^{im\phi}=\sum_{l=l_{\min}}^{\infty}b^l_{\hat{l}m}(\sigma^2)Y_{lm}(\theta,\phi), \tag{A2}$$

where $l_{\min}=|m|$. In order to calculate the coefficients $b^l_{\hat{l}m}$ we substitute this expansion into Eq. (A1). Noting that the Y_{lm} satisfy (A1) when $\sigma=0$ with $\lambda_{lm}=l(l+1)$, we get

$$\sum_{l=l_{\min}}^{\infty}b^l_{\hat{l}m}[\sigma^2\cos^2\theta+l(l+l)]Y_{lm}=\lambda_{\hat{l}m}\sum_{l=l_{\min}}^{\infty}b^l_{\hat{l}m}Y_{lm}. \tag{A3}$$

Next we multiply the above expression by $Y^*_{\hat{l}m}$ and integrate over the sphere. The resulting inner products are given by

$$\oint Y^*_{\hat{l}m}Y_{lm}d\Omega=\delta_{\hat{l}l}, \tag{A4}$$

$$\oint Y^*_{\hat{l}m}\cos^2\theta Y_{lm}d\Omega=\frac{1}{3}\delta_{\hat{l}l}+\frac{2}{3}\sqrt{\frac{2l+1}{2\hat{l}+1}}\langle l,2,m,0|\hat{l},m\rangle\times\langle l,2,0,0|\hat{l},0\rangle\equiv k^l_{\hat{l}m}. \tag{A5}$$

Here the numbers $\langle j_1,j_2,m_1,m_2|jm\rangle$ are standard Clebsch-Gordan coefficients, the form of which implies that $k^l_{\hat{l}m}\neq 0$ only for $l\in\{\hat{l}-2,\hat{l}-1,\hat{l},\hat{l}+1,\hat{l}+2\}$. Consequently, Eq. (A3) reduces to the recursion relation

$$\sigma^2k^{\hat{l}-2}_{\hat{l}m}b^{\hat{l}-2}_{\hat{l}m}+\sigma^2k^{\hat{l}-1}_{\hat{l}m}b^{\hat{l}-1}_{\hat{l}m}+[\sigma^2k^{\hat{l}}_{\hat{l}m}+l(l+1)]b^{\hat{l}}_{\hat{l}m}+\sigma^2k^{\hat{l}+1}_{\hat{l}m}b^{\hat{l}+1}_{\hat{l}m}+\sigma^2k^{\hat{l}+2}_{\hat{l}m}b^{\hat{l}+2}_{\hat{l}m}=\lambda_{\hat{l}m}b^{\hat{l}}_{\hat{l}m} \tag{A6}$$

for the expansion coefficients $b^l_{\hat{l}m}$ (with given $\hat{l}$, m). This can be put in a matrix form, $K\mathbf{b}=\lambda\mathbf{b}$ (keeping the indices $\hat{l}$, m implicit), where K is a known band-diagonal matrix (made up of the known σ^2 and $k^l_{\hat{l}m}$) and $\mathbf{b}=(b^{\hat{l}=1}_{\hat{l}m},b^{\hat{l}=2}_{\hat{l}m},\ldots)$. This is a standard eigenvalue problem for the eigenvectors $\mathbf{b}$ and eigenvalues λ (for each $\hat{l}$, m), and the band-diagonality of K makes it readily amenable to numerical treatment. This method of obtaining the expansion coefficients $b^{\hat{l}}_{\hat{l}m}$ and spheroidal-harmonic eigenvalues $\lambda_{\hat{l}m}$, which we adopt in this work, follows closely that of Hughes in [34].

APPENDIX B: REGULARIZATION PARAMETERS IN KERR GEOMETRY

The regularization parameters for the SSF in a generic orbit about a Kerr black hole were calculated by Barack and Ori in Ref. [30] (see [2] for a detailed derivation). For circular-equatorial orbits they reduce to

$$C_\mu=D_\mu=0, \tag{B1}$$

and (in Boyer-Lindquist coordinates)

$$A^\pm_r=\mp q^2\Delta^{-1/2}(g_{\phi\phi}+\mathcal{L}^2)^{-1/2}, \tag{B2}$$

$$A^\pm_t=A^\pm_\theta=A^\pm_\phi=0, \tag{B3}$$

where the metric function $g_{\phi\phi}$ is evaluated on the equatorial orbit. The expression for B_μ is more complicated. It can be written in the form

$$B_\mu=q^2P_{\mu abcd}I^{abcd}, \tag{B4}$$

where hereafter Roman indices run over the two Boyer-

Lindquist angular coordinates θ, ϕ only. The coefficients $P_{\mu abcd}$ are given by

$$P_{\mu abcd} = (4\pi)^{-1}[3P_{\mu d}P_{abc} - (2P_{\mu ab} + P_{ab\mu})P_{cd}], \tag{B5}$$

where

$$P_{\alpha\beta} \equiv g_{\alpha\beta} + u_\alpha u_\beta, \tag{B6}$$

$$P_{\alpha\beta\gamma} \equiv (u_\lambda u_\gamma \Gamma^\lambda_{\alpha\beta} + g_{\alpha\beta,\gamma}/2), \tag{B7}$$

with the Kerr connections $\Gamma^\lambda_{\alpha\beta}$ and metric functions $g_{\alpha\beta}$ all evaluated on the equatorial orbit. The quantities I^{abcd} are

$$I^{abcd} = \int_0^{2\pi} G(\gamma)^{-5/2}(\sin\gamma)^N(\cos\gamma)^{4-N}d\gamma, \tag{B8}$$

where

$$G(\gamma) \equiv P_{\phi\phi}\sin^2\gamma + 2P_{\theta\phi}\sin\gamma\cos\gamma + P_{\theta\theta}\cos^2\gamma, \tag{B9}$$

and $N \equiv N(abcd)$ is the number of times the index ϕ occurs in the combination (a, b, c, d), namely,

$$N = \delta^a_\phi + \delta^b_\phi + \delta^c_\phi + \delta^d_\phi. \tag{B10}$$

The quantities I^{abcd} can be written explicitly in terms of complete elliptic integrals [2,30]. In the case of a circular-equatorial orbit these expressions become

$$I^{abcd} = \frac{2(1-w)I^{(N)}_K\hat{K}(w) + I^{(N)}_E\hat{E}(w)}{24P^{5/2}_{\phi\phi}w^4(1-w)^2}, \tag{B11}$$

where $\hat{K}(w) \equiv \int_0^{\pi/2}(1 - w\sin^2x)^{-1/2}dx$ and $\hat{E}(w) \equiv \int_0^{\pi/2}(1 - w\sin^2x)^{1/2}dx$ are complete elliptic integrals of the first and second kinds, respectively, and

$$w \equiv 1 - \frac{P_{\theta\theta}}{P_{\phi\phi}}. \tag{B12}$$

The coefficients $I^{(N)}_K$ and $I^{(N)}_E$ are given by

$$\begin{aligned}
&I^{(0)}_K = 16w^2(2-3w), \qquad I^{(0)}_E = 64w^2(2w-1),\\
&I^{(1)}_K = I^{(1)}_E = 0, \qquad I^{(2)}_K = 32w^2(w-1),\\
&I^{(2)}_E = 32w^2(w^2-3w+2), \qquad I^{(3)}_K = I^{(3)}_E = 0,\\
&I^{(4)}_K = -16w^2(w^2+w-2),\\
&I^{(4)}_E = -64w^2(w^3-w^2-w+1).
\end{aligned} \tag{B13}$$

APPENDIX C: BOUNDARY CONDITIONS FOR THE RADIAL SCALAR-FIELD EQUATION

In order to derive recurrence relations for the asymptotic expansion coefficients c^∞_l and c^{eh}_k in Eqs. (36) and (37), we substitute these equations into the homogeneous part of the radial equation (20). By comparing the coefficients of r^{-k} (at infinity) or $(r - r_+)^k$ (at the event horizon) we obtain five-term recurrence relations for each of $c^\infty_{k>0}$ and $c^{eh}_{k>0}$. Setting $c^{\infty,eh}_{k<0} = 0$ and $c^{\infty,eh}_{k=0} = 1$ allows us to determine all coefficients $c^{\infty,eh}_{k>0}$ in a recursive fashion.

Explicitly, the above recurrence relations are given by

$$\sum_{i=0}^{5} f^\infty_i c^\infty_{k-i} = 0, \qquad \sum_{i=0}^{5} f^{eh}_i c^{eh}_{k-i} = 0, \tag{C1}$$

where the various coefficients f^∞_i and f^{eh}_i read

$$\begin{aligned}
&f^\infty_0 = -2k\omega_m i, \qquad f^\infty_1 = k^2 - \lambda_{\hat{l}m} + \omega_m(a^2\omega_m - 4iM) + k(4iM\omega_m - 1),\\
&f^\infty_2 = 2[ia^2(2-k)\omega_m + M(a^2\omega^2_m - 2am\omega_m - 2k^2 + 5k - 3 + \lambda_{\hat{l}m})],\\
&f^\infty_3 = 4(k-2)^2M^2 - a^2(\lambda_{\hat{l}m} - 2k^2 + 8k - 8 - m^2), \qquad f^\infty_4 = -2a^2M(2k^2 - 11k + 15), \qquad f^\infty_5 = a^4(k^2 - 7k + 12),
\end{aligned} \tag{C2}$$

$$\begin{aligned}
f^{eh}_0 = {}& -a^4[k^2 + k(-3 - 4ir_+\omega_m) - r^2_+\omega^2_m + 2] + 2a^3mr_+(r_+\omega_m + 2ik) - a^2r_+[2M(6k^2 + k(-12 - 6ir_+\omega_m)\\
&- r^2_+\omega^2_m + 3) + r_+(-12k^2 + 2k(9 + 8ir_+\omega_m) + r^2_+\omega^2_m + \lambda_{\hat{l}m} - 2)] + 2amr^2_+[r_+\omega_m(r_+ - 2M) - 2ik(3M - 2r_+)]\\
&+ r^2_+[4(6k^2 - 9k + 1)M^2 + 2Mr_+(-20k^2 + 10ikr_+\omega_m + 24k + \lambda_{\hat{l}m} - 1) + r^2_+(15k^2 - 12ikr_+\omega_m - 15k - \lambda_{\hat{l}m})],\\
f^{eh}_1 = {}& 2\{a^4\omega_m(ik + r_+\omega_m - i) - ia^3m(k - 2ir_+\omega_m - 1) + a^2M[2k^2 - k(9 + 6ir_+\omega_m) - 3r^2_+\omega^2_m + 6ir_+\omega_m + 10]\\
&+ a^2r_+[-4k^2 + 3k(5 + 4ir_+\omega_m) + 2r^2_+\omega^2_m - 12ir_+\omega_m + \lambda_{\hat{l}m} - 13] + 2amr_+[3M(ik + r_+\omega_m - i)\\
&+ r_+(-3ik - 2r_+\omega_m + 3i)] + r_+(-8k^2 + 30k - 26)M^2 + Mr^2_+(20k^2 - 20ikr_+\omega_m - 66k + 20ir_+\omega_m - 3\lambda_{\hat{l}m} + 49)\\
&+ r^3_+(-10k^2 + 15ikr_+\omega_m + 30k - 15ir_+\omega_m + 2\lambda_{\hat{l}m} - 20)\},
\end{aligned} \tag{C3}$$

$$f_2^{eh} = a^4\omega_m^2 - 2a^3 m\omega_m + a^2[-2k^2 + 4k(-iM\omega_m + 4ir_+\omega_m + 3) - 6Mr_+\omega_m^2 + 8iM\omega_m + 6r_+^2\omega_m^2 - 32ir_+\omega_m + \lambda_{\hat{l}m} - 18] + 4iam[M(k - 3ir_+\omega_m - 2) + r_+(-2k + 3ir_+\omega_m + 4)] + 2Mr_+(10k^2 - 20ikr_+\omega_m - 54k + 40ir_+\omega_m - 3\lambda_{\hat{l}m} + 71) + r_+^2(-15k^2 + 40ikr_+\omega_m + 75k - 80ir_+\omega_m + 6\lambda_{\hat{l}m} - 90) - 4(k-3)^2M^2,$$

$$f_3^{eh} = -2a^2\omega_m(-2ik + M\omega_m - 2r_+\omega_m + 6i) + 2am(-ik + 2M\omega_m - 4r_+\omega_m + 3i) + M[4k^2 - k(30 + 20ir_+\omega_m) + 60ir_+\omega_m - 2\lambda_{\hat{l}m} + 56] + 2r_+[-3k^2 + 3k(7 + 5ir_+\omega_m) - 45ir_+\omega_m + 2\lambda_{\hat{l}m} - 36],$$

$$f_4^{eh} = a^2\omega_m^2 - 2am\omega_m - k^2 + k(-4iM\omega_m + 12ir_+\omega_m + 9) + 16iM\omega_m - 48ir_+\omega_m + \lambda_{\hat{l}m} - 20,$$

$$f_5^{eh} = 2i(k-5)\omega_m.$$

[1] LISA website, http://lisa.nasa.gov/.
[2] L. Barack, Classical Quantum Gravity **26**, 213001 (2009).
[3] Y. Mino, M. Sasaki, and T. Tanaka, Phys. Rev. D **55**, 3457 (1997).
[4] T. C. Quinn and R. M. Wald, Phys. Rev. D **56**, 3381 (1997).
[5] S. Detweiler and B. F. Whiting, Phys. Rev. D **67**, 024025 (2003).
[6] S. E. Gralla and R. M. Wald, Classical Quantum Gravity **25**, 205009 (2008).
[7] A. Pound, Phys. Rev. D **81**, 024023 (2010).
[8] A. I. Harte, arXiv:0910.4614.
[9] E. Poisson, Living Rev. Relativity **7**, 6 (2004).
[10] B. S. Dewitt and R. W. Brehme, Ann. Phys. (N.Y.) **9**, 220 (1960).
[11] J. M. Hobbs, Ann. Phys. (N.Y.) **47**, 141 (1968).
[12] S. E. Gralla, A. I. Harte, and R. M. Wald, Phys. Rev. D **80**, 024031 (2009).
[13] T. C. Quinn, Phys. Rev. D **62**, 064029 (2000).
[14] L. Barack and A. Ori, Phys. Rev. D **61**, 061502 (2000).
[15] L. Barack and L. M. Burko, Phys. Rev. D **62**, 084040 (2000).
[16] L. M. Burko, Phys. Rev. Lett. **84**, 4529 (2000).
[17] L. M. Diaz-Rivera, E. Messaritaki, B. F. Whiting, and S. Detweiler, Phys. Rev. D **70**, 124018 (2004).
[18] R. Haas, Phys. Rev. D **75**, 124011 (2007).
[19] R. Haas, Proceedings of the 11th Capra Meeting, Orleans, 2008.
[20] L. Barack and C. O. Lousto, Phys. Rev. D **66**, 061502 (2002).
[21] L. Barack and N. Sago, Phys. Rev. D **75**, 064021 (2007).
[22] S. Detweiler, Phys. Rev. D **77**, 124026 (2008).
[23] L. Barack and N. Sago, arXiv:1002.2386 [Phys. Rev. D (to be published)].
[24] L. Barack, D. A. Golbourn, and N. Sago, Phys. Rev. D **76**, 124036 (2007).
[25] C. O. Lousto and H. Nakano, Classical Quantum Gravity **25**, 145018 (2008).
[26] I. Vega, P. Diener, W. Tichy, and S. Detweiler, Phys. Rev. D **80**, 084021 (2009).
[27] C. O. Lousto, H. Nakano, Y. Zlochower, and M. Campanelli, arXiv:0910.3197 [Phys. Rev. D (to be published)].
[28] J. L. Blum, J. M. Miller, A. C. Fabian, M. C. Miller, J. Homan, M. van der Klis, E. M. Cackett, and R. C. Reis, Astrophys. J. **706**, 60 (2009).
[29] L. Barack and N. Sago, Phys. Rev. Lett. **102**, 191101 (2009).
[30] L. Barack and A. Ori, Phys. Rev. Lett. **90**, 111101 (2003); see arXiv:gr-qc/0212103v1 or [2] for the explicit expressions of the regularization parameters in terms of elliptic integrals.
[31] L. Barack, A. Ori, and N. Sago, Phys. Rev. D **78**, 084021 (2008).
[32] S. E. Gralla, J. L. Friedman, and A. G. Wiseman, arXiv:gr-qc/0502123.
[33] D. V. Gal'tsov, J. Phys. A **15**, 3737 (1982).
[34] S. A. Hughes, Phys. Rev. D **61**, 084004 (2000).
[35] L. M. Burko, A. I. Harte, and E. Poisson, Phys. Rev. D **65**, 124006 (2002).
[36] B. Carter, Phys. Rev. **174**, 1559 (1968).
[37] D. R. Brill, P. L. Chrzanowski, C. M. Pereira, E. D. Fackerell, and J. R. Ipser, Phys. Rev. D **5**, 1913 (1972).
[38] J. M. Bardeen, W. H. Press, and S. A. Teukolsky, Astrophys. J. **178**, 347 (1972).
[39] E. Poisson, *A Relativist's Toolkit: The Mathematics of Black-Hole Mechanics* (Cambridge University Press, Cambridge, England, 2004).
[40] S. Chandrasekhar, *The Mathematical Theory of Black Holes* (Oxford University Press, New York, 1992), Chap. 58.
[41] V. P. Frolov and I. D. Novikov, *Black Hole Physics* (Kluwer Academic Publishers, Dordrecht, 1998).
[42] L. Barack, Y. Mino, H. Nakano, A. Ori, and M. Sasaki, Phys. Rev. Lett. **88**, 091101 (2002).
[43] S. R. Dolan, Ph.D. thesis, Cambridge, 2007.
[44] Gnu Scientific Library, http://www.gnu.org/software/gsl/.
[45] R. Haas and E. Poisson, Phys. Rev. D **74**, 044009 (2006).
[46] W. Hikida, H. Nakano, and M. Sasaki, Classical Quantum Gravity **22**, S753 (2005).
[47] T. Damour and G. Esposito-Farèse, Phys. Rev. D **53**, 5541 (1996).
[48] S. Detweiler, E. Messaritaki, and B. F. Whiting, Phys. Rev. D **67**, 104016 (2003).
[49] Note our definition of the scalar field differs from that of Hikida *et al.* [46] by a factor 4π, leading to a similar relative factor in the SSF.